

SPIONs doped with cobalt from the Li-ion battery acid leaching waste as a photocatalyst for tetracycline degradation – synthesis, characterization, DFT studies, and antibiotic treatment

Paulina Pietrzyk-Thel^{a,†,*}, Magdalena Osial^{a,†,*}, Agnieszka Pregowska^a, Magdalena Abramowicz^b, Thu Phuong Nguyen^c, Weronika Urbańska^d, Michael Giersig^a

^a*Institute of Fundamental Technological Research, Polish Academy of Sciences, Pawlowskiego 5B Street, 02-106 Warsaw, Poland, emails: ppietrz@ippt.pan.pl (P. Pietrzyk-Thel), mosial@ippt.pan.pl (M. Osial), aprego@ippt.pan.pl (A. Pregowska), mgiersig@ippt.pan.pl (M. Giersig)*

^b*Faculty of Chemistry, University of Warsaw, Pasteura 1 Street, 02-093 Warsaw, Poland, email: m.abramowicz8@student.uw.edu.pl*

^c*Institute for Tropical Technology, Vietnam Academy of Science and Technology, 18 Hoang Quoc Viet, Cau Giay District, Hanoi 10000, Vietnam, email: ntpuong@itt.vast.vn*

^d*Faculty of Environmental Engineering, Wrocław University of Science and Technology, Wybrzeże Wyspiańskiego 27 Street, 50-370 Wrocław, Poland, email: weronika.urbanska@pwr.edu.pl*

Received 7 February 2023; Accepted 19 July 2023

ABSTRACT

This work demonstrates the removal of cobalt-containing liquid waste recovered from spent lithium-ion battery waste in the context of the synthesis of superparamagnetic particles and their application for tetracycline photodegradation. First, the spent lithium-ion battery waste was treated with H₂SO₄, glutaric acid and H₂O₂ to release heavy material from the graphite electrodes, and then the post-acid leaching solution was used as a source of Co²⁺ ions in the wet co-precipitation synthesis of superparamagnetic co-doped iron oxide nanoparticles. Scanning electron microscopy and transmission electron microscopy revealed the spherical morphology of nanoparticles with a size of 15 ± 4.80 nm. Fourier-transform infrared spectroscopy and X-ray diffraction confirmed the formation of iron oxide doped with Co, while the particles obtained have a polycrystalline structure. Magnetometric measurements prove the superparamagnetic properties of the obtained material with saturation magnetization (*M_s*) of about 91 emu/g. The band gap energy estimated from Tauc plot for obtained nanoparticles is about 1.6 eV, while the flat band potential calculated from Mott–Schottky's plot is about –0.18 V vs. SHE. The experimental studies conducted with UV-Vis show the highest efficacy in pH 7 degradation of tetracycline (TC) of about ~84.42%, with the process undergoing first-order kinetics. The addition of H₂O₂ improves the effectiveness to reach about 92.2% TC degradation. It turned out that magnetic nanoparticles from waste battery waste have catalytic properties and can be considered efficient catalysts in various fields, including environmental studies. The material obtained provides reuse for 5 operating cycles and can be easily removed from aqueous media after effective treatment.

Keywords: Spent lithium-ion batteries; LiBs; Acid leaching; SPION; Magnetic nanomaterials; Metals recovery; Superparamagnetic; Waste management; Functional materials

* Corresponding authors.

† These authors contributed equally to this work.

1. Introduction

As an effect of climate policy targets and actions taken to reduce the carbon footprint and the associated increased production of hybrid and electric vehicles, the manufacturing of energy storage devices, particularly Li-ion batteries (LiBs), rapidly grew. It is connected with their higher effectiveness. On the other hand, these types of spent batteries contain many different metals, such as lithium, cobalt, manganese, nickel, copper, or aluminum, as well as toxic organic electrolytes [1–3].

Thus, the spent batteries are the source of both secondary critical metals and environmental pollutants [4]. Consequently, the hazardous waste that contains harmful chemical substances and metal ions is also growing [5]. They also increase the environmental burden due to the shorter life span compared to other battery types [6]. In addition, the trend related to electromobility and the widespread use of hybrid and electric cars is relatively new. Therefore, the amount of spent Li-ion batteries from the automotive industry can be expected to increase dramatically only over the next several years.

Due to their complex chemical composition, waste Li-ion batteries should be collected selectively and subjected to appropriate recycling processes [7,8]. Improper disposal of battery waste can lead to the penetration of heavy metal ions into the water and soil environment, thus creating a threat to the health of humans and animals as well as the condition of plants. It has been shown that high levels of lithium are toxic for both aquatic animals and humans [9]. In turn, lithium released into the soil environment may contribute to soil dispersion and aggregate swelling. It gets to the plants through the soil and then goes to the organisms that consume them [10–12]. In turn, a high level of nickel contributes to homeostasis disruption [13]. Copper, which is included in the food, affects the liver and gastric states [14,15]. Another threat resulting from improper Li-ion batteries' improper storage is their possible self-ignition and causing dangerous fires and explosions [16,17]. Thus, disposal and recycling of spent LiBs remain a challenge, as most of them end their life cycles in landfills and then contaminate soil and water [18]. Moreover, in contrast to the growing demand for LiBs, the actual recovery rate of spent batteries is low [9].

The currently used industrial technologies for recycling waste LiBs focus mainly on recovering critical metals from maintaining the current technological level, that is, lithium and cobalt. Hydrometallurgical and/or pyrometallurgical processes can recover these elements with prior mechanical treatment [19]. The hydrometallurgical process, in comparison to the pyrometallurgical process, is characterized by low energy consumption, and low CO₂ emission, while it generates low pH solid and liquid by-products, which require economically costly neutralization and further management [8]. Thus, the most frequently used reagents in the hydrometallurgical recovery of metals from spent batteries are leaching acids – inorganic and organic with reducing agents, in particular hydrogen peroxide and ascorbic acid [20–22]. Especially organic acids are environmentally friendly leaching agents in the case of Li and Co recovery processes [23]. Organic acids dominate in the recovery of Co, while the inorganic ones in Li. Organic acids require

a higher solid-to-liquid ratio than inorganic acids [24]. In turn, in the case of organics agents, only the leaching kinetics has been widely explored [25], while other leaching aids, as well as the application of organics agents like formic, propionic, butyric, glycolic, gallic, and gluconic, still need to be examined [26,27]. An alternative to hydrometallurgy and pyrometallurgy is biological processes that use the potential of extremophilic microorganisms to live in an acidic environment contaminated with metals [28]. The advantage of waste LiBs bioleaching is the effects comparable to chemical leaching and thermal processes, with less environmental damage (elimination of pollutant emissions, generation of additional solid waste or acid effluents). However, due to the long reaction time, poor adaptability of microbes, and rigorous leaching conditions, this method is still the subject of laboratory research and requires detailed optimization before being introduced into industrial practice [29]. Moreover, materials contained in spent Li-ion batteries can also be regenerated in the so-called direct recycling, where the obtained materials' value is related to their type [6,30].

As already mentioned, all spent battery recycling processes generate secondary waste that requires further management [8]. In accordance with the principles of the circular economy, the sustainable use of raw materials and their recovery from waste is the basic task of modern economic systems [31,32]. Therefore, in all technologies, including recycling, it is important to manage all types of produced waste, including secondary waste generated during the processing of used materials, for example, in hydrometallurgical processes the management of the obtained acidic, polymetallic solutions. In the first place, metals are selectively recovered from them, most often using chemical methods – precipitation, solvent extraction, or ion flotation [33]. Nevertheless, these processes still do not lead to the full recovery of all metals, therefore, even after the selective separation of some elements, there is still a problem with the management of the liquid residue containing various metals and chemical compounds. Thus, the production of nanomaterials based on waste-derived compounds may provide a practical and efficient solution to waste management issues, in particular in the field of the LiBs recycling process [34]. This leads to a double benefit, on the one hand, waste-derived nanoparticles will reduce the use of limited raw resources and on the other hand provide environmentally friendly physico-chemical technologies of nanoparticle synthesis [35].

Since the magnetic nanoparticles can be easily separated from the solution under the external magnetic field, they can be extensively studied as an effective adsorbent of impurities from water, especially of pharmaceutical origin [36–40]. The advantages of such an approach are simplicity of the process and operation, long-term stability in the wide pH range, low manufacturing costs, high efficiency and environmental friendliness compared to other methods [41].

The great advantage of this technology is the possibility of using various types of industrial waste, household waste, and agricultural waste. Depending on the type, the magnetic nanoparticles enable the removal of different pollutants from water, including substances of pharmaceutical origin, dyes, and organic compounds such as methyl blue, phenol, and phenanthrene [42,43].

For example, carbon-based magnetic nanoparticles made from rice husk waste can remove Cd(II) from water [44]. Sahib et al. [45], a graphene oxide-based magnetic adsorbent was applied to Alizarin Red S (ARS) dye removal, Azam et al. [46], the graphene oxide-based adsorbent, which was received from waste dry cell battery to Pb removal from water, was proposed. Another interesting study by Zou et al. [47] presented the spent LiBs-based zeolite for heavy metal removal showing the potential of spent battery waste material in environmental studies. Besides the magnetic separation, iron oxide-based adsorbents also offer photocatalytic performance for their semiconducting properties. Therefore, they are widely used not only for removal but also photo-driven degradation of contaminants in aquatic reservoirs [48], for example, dyes like AR206 [49], Congo red [50], indigo carmine [51]; pharmaceuticals like tetracycline (TC) [52], tamoxifen [53], ceftriaxone and amoxicillin [54], levofloxacin [55], metronidazole [56], sulfathiazole [57]; or other pollutants like pentachlorophenol [58], phenol [59].

In this article, we consider secondary battery waste as a source of valuable metals that can be used as a source for the synthesis of functional material, especially photocatalysts for wastewater treatment. Since the spent LiBs are a challenge for the handling of materials, especially when it comes to the secondary waste generated during acid leaching, we demonstrate here their ease of use by providing magnetic nanoparticles. Acid leaching solutions (ALS) from LiBs treatment were used as a co-source during wet synthesis of the superparamagnetic iron oxide-based nanoparticle. Subsequently, the materials obtained were characterized to determine the morphology, chemical composition, magnetic and optical properties. In addition, nanoparticles have been used to treat one of the most common water pollutants – tetracycline (TC). It turned out that magnetic nanoparticles from waste have catalytic properties and can be considered efficient catalysts in water treatment, in particular in the case of antibiotics removal. And in this way, hazardous solutions do not become useless and waste challenging to process but constitute the raw material for further use. As a consequence, the circulation of valuable materials may be closed. The paper is organized as follows: In Section 2, we briefly describe the materials and methods. Section 3 presented the experimental results, including acid leaching of waste battery powder, morphology, chemical composition, and photodegradation, magnetic and optical properties studies, as well as the density functional theory (DFT) calculation for tetracycline. Section 4 contains a discussion, some concluding remarks, and some direction for future development.

2. Materials, methods, and procedures

2.1. Materials

First, the stream of spent Li-ion battery (18650 type) was discharged and dismantled mechanically to separate the particular components following the procedure described previously [21]. Then, the battery powder from spent anode and cathode was washed several times with distilled water to remove the electrolyte from the electrodes, filtered to

separate the residue from the solution and dried in 50°C overnight. Next, the spent battery powder was subjected to mineralization using the nitric acid HNO₃ 65% (POCH, Poland) to determine the initial quantitative and qualitative composition. For the leaching experiments, battery powder was used without prior additional chemical and/or thermal treatment. As a leaching agent, the sulfuric acid H₂SO₄ with 96% analytical grade was used. Additionally, the reducing agent – hydrogen peroxide H₂O₂ with 30% analytical grade (STANLAB, Lublin, Poland) was also dosed at the beginning of the leaching process. In turn, next, the battery waste powder was used as a dopant during the co-precipitation method. The iron(III) chloride hexahydrate FeCl₃·6H₂O (analytical grade) was purchased from Warchem, Warsaw, Poland, and iron(II) chloride tetrahydrate FeCl₂·4H₂O for UV-Vis studies was supplied from Acros Organics (Geel, Belgium). The cobalt(II) sulfate(VI) heptahydrate CoSO₄·7H₂O with analytical grade was also purchased from Warchem, Warsaw, Poland. These salts were used for the synthesis of iron oxide-based nanoparticles. 25% aqueous ammonia solution NH₃(aq) that was applied to precipitate nanoparticles from the iron salt-based solution was supplied from POCH, Poland. The tetracycline C₂₂H₂₄N₂O₈ used as a model pollutant was purchased from Sigma-Aldrich, Berlin, Germany.

2.2. Methods

The morphology of obtained nanomaterials was studied with Scanning Electron Microscope (SEM, Hitachi S-4800, Japan) and Transmission Electron Microscope (TEM, JEM 1400-Flash, JEOL, Japan). Magnetic properties of nanomaterials were studied with a homemade vibrating sample magnetometer under the maximum applied field of 15 kOe at room temperature. Fourier-transform infrared (FTIR) spectra of samples were recorded by Nicolet iS10 FTIR Spectrometer, Thermo Scientific (Massachusetts, USA). X-ray diffraction was obtained by D8 Advance - Bruker AXS GmbH (Karlsruhe, Germany), CuK α radiation ($\lambda = 1.54056 \text{ \AA}$) with a step angle of 0.030°, the scanning rate of 0.04285°/s, and 2 θ degrees in the range of 15°–70°. The UV-Vis spectra were measured using PerkinElmer Lambda 1050+ (Pro-environment, Poland), the measurements were in a quartz cuvette of the length of the optical beam 1 cm. The spectra were measured in the range of wavelength 250–800 nm. As a UV-Vis light, the 280 W mercury quartz lamp PLK-5 (POLAMP, Warsaw, Poland, emission spectrum ranging from 180 to 623 nm) with was used.

2.3. Acid leaching of waste battery powder

The first step was based on the acid leaching of the spent battery waste. Here, the acid leaching was performed in 1.5 M sulfuric acid (96% analytical grade, STANLAB, Lublin, Poland), as the reducing agents glutaric acid C₅H₈O₄ (5% w/v) and hydrogen peroxide H₂O₂ (30% analytical grade, STANLAB, Lublin, Poland; 0.9% v/v) based on the acid leaching procedure described by the study of Urbańska [21], where also the recovery rate of the particular metals was estimated. The applied process conditions allowed for the effective transfer of metals from the electrode powder into polymetallic solutions with a low pH (approx. pH 1). Such solutions can be used for further selective separation of individual

metals, but still, in the end, they will require appropriate neutralization due to the complex chemical composition and acidic pH. Otherwise, in the event of improper management, they constitute very hazardous waste for the soil and water environment and for living organisms. The obtained ALS was used in the following step as a source of cobalt ions, where the acids were completely neutralized during the subsequent co-precipitation technique. Therefore, not only the cobalt was recovered, but also instead of the acidic product, the salts were obtained, in particular chlorides and sulfates that can be easily crystallized and removed from water.

The synthesis of iron-oxide-based nanoparticles as an effective way of liquid battery waste management was performed as follows. The precipitation was performed in the 100 mL glass beaker, where the 1.08 g of $\text{FeCl}_3 \cdot 6\text{H}_2\text{O}$ dissolved in 40 mL of distilled Milli-Q water. Then, the solution was stirred at 600 rpm until the dissolution of the salt, and the 380 mg of $\text{FeCl}_2 \cdot 4\text{H}_2\text{O}$ was added and continuously stirred. Subsequently, 1 mL of the ALS was added dropwise, and the prepared solution was heated up to 70°C for 5 min. Next, the 25% $\text{NH}_3(\text{aq})$ solution was added dropwise towards precipitation. It was added until pH 10.5 – 11, and the suspension was intensively stirred at 1000 rpm for 15 min. Afterward, the obtained nanoparticles were collected at the bottom of the beaker with a magnet and washed with Milli-Q water several times until the neutral pH. The mass of the final product was about 460 ± 10 mg. Fig. 1 shows the schematic diagram of the second life of the battery waste – from harmful battery waste powder to the functional material. The pink color of the post-acid leaching waste solution is mainly caused by the presence of the Co^{2+} ions.

3. Results

3.1. Morphology studies

The material obtained with co-precipitation in the presence of ALS in the bath was investigated with scanning electron microscopy (SEM) and transmission electron microscopy (TEM) to determine its morphology. SEM delivers general information about the morphology, while the samples overlap each other due to the drying. Therefore, TEM was used to determine the shape and size of nanoparticles. Based on the SEM image presented in Fig. 2a the morphology of superparamagnetic iron oxide-based nanoparticles (SPIONs) resembles a grainy structure and spherical shape similar to the morphology of the iron-oxide-based nanoparticles presented in the literature [60,61]. The average diameter of nanoparticles is approximately 15 ± 4.80 nm (Fig. 2b).

3.2. Chemical composition studies

Before synthesizing iron oxide-based nanoparticles, the ALS was measured with UV-Vis spectrometry to determine the concentration of cobalt ions in the solution, Fig. 3a. The set of reference solutions with different Co^{2+} content was measured to determine these ions concentrations in the ALS bath. The blue curve corresponds to the reference solution of 0.045 M CoSO_4 solution. Based on the reference measurements, the concentration of Co^{2+} in the ALS for synthesizing nanomaterials is approx. 0.05 M. As can be seen, the spectrum for the ALS used for the synthesis, before Fe(II) and Fe(III) salts addition, has a similar shape

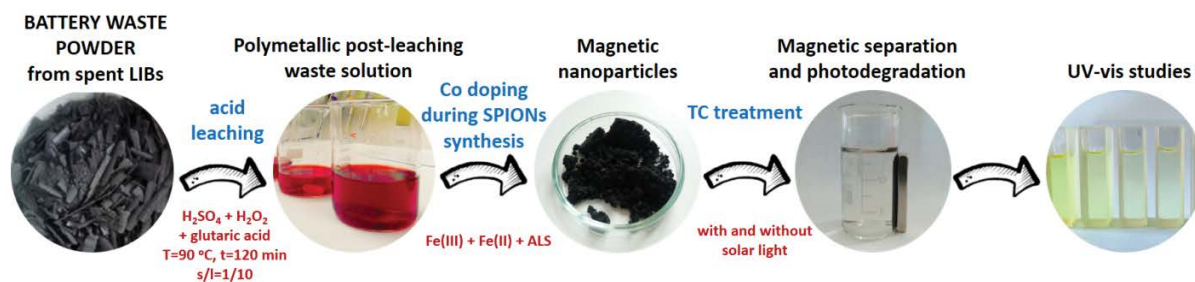


Fig. 1. Schematic diagram of the acid leaching solution use towards the second life of the battery waste.

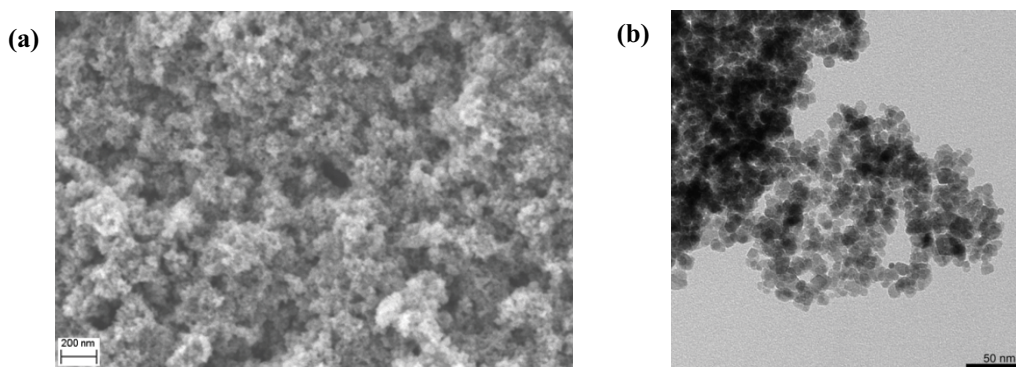


Fig. 2. (a) Scanning electron microscopy image and (b) transmission electron microscopy image of the obtained nanoparticles.

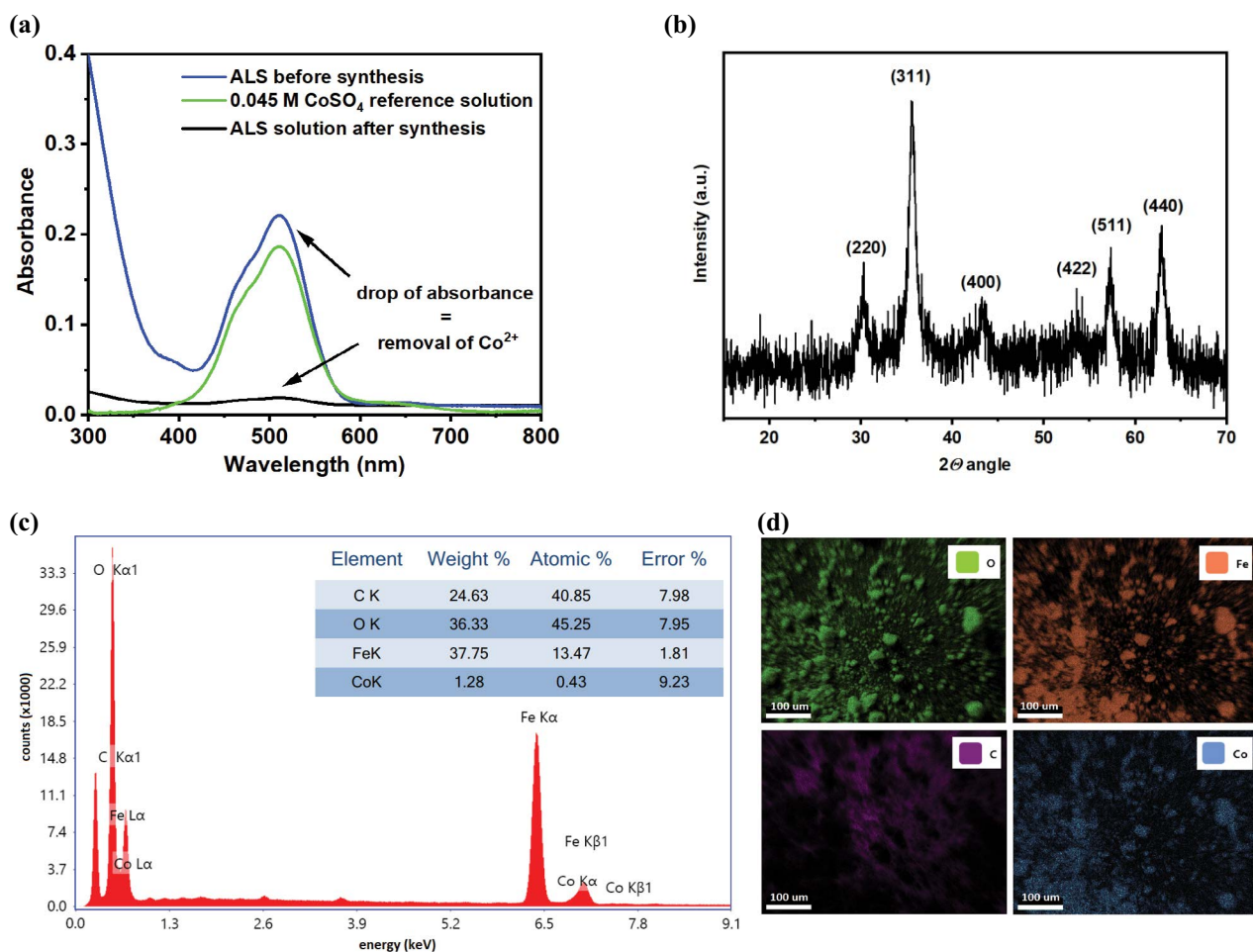


Fig. 3. (a) UV-Vis spectrum of acid leaching solution before and after the synthesis of nanostructures, (b) X-ray diffraction pattern for as-synthesized nanoparticles, and (c) energy-dispersive X-ray spectrum for sample 1, and (d) maps presenting elements (Fe, Co, O, and C) distribution.

to the curves presented elsewhere, revealing the broadband of about 500 nm [62]. Subsequently, the UV spectra were measured after the synthesis of nanoparticles, where the obtained material was separated magnetically from the solution. It is seen that the absorbance of the cobalt in post-synthesis ALS drastically drops, which confirms the removal of Co²⁺ through its incorporation into the nanoparticles. Obtained results are in good agreement with the recorded energy-dispersive X-ray spectroscopy (EDS) maps. Complementary to the EDS mapping, the chemical composition was also investigated with the other techniques. Obtained nanoparticles were characterized in respect of crystallinity using the X-ray diffraction technique (XRD). As shown in Fig. 3b the diffractogram of iron nanoparticles doped with cobalt is seen. The sample mainly consists of the peaks at 30.22°, 35.57°, 43.25°, 53.54°, 58°, and 62.94° corresponding to the (220), (311), (400), (422), (511), and (440) planes of a cubic spinel-type structure CoFe₂O₄ (JCPDS no. 79-1744). Similar results are presented in the literature [63,64], while these peaks also may correspond to the inverted spinel-space group Fd-3m of Fe₃O₄ [65].

The crystallite size D was estimated using the Scherrer formula [66]:

$$D = \lambda K (\beta (\cos \theta))^{-1} \quad (1)$$

where the β stands for the full width-at-half-maximum length of the reflection, θ is the Bragg angle, λ is the X-ray wavelength, and k is a dimensionless shape factor (0.94). The calculated size of crystallites is about 16.83 ± 1.80 nm. The result of TEM confirms the size from nanoparticles obtained to calculate crystallites, which is similar to the present of literature [67].

Complementary to the XRD analysis, the EDS spectrum and the maps presenting the elemental composition of the sample were recorded. The spectrum revealing the peaks for iron, oxide, carbon, and oxygen, is demonstrated in Fig. 3c. Following image in Fig. 3d shows the distribution of particular elements in the sample. As can be seen, the cobalt is uniformly distributed in the all sample. The carbon mainly comes from the carbon tape that was used to immobilize particles for EDS analysis. Therefore, with EDS the determination of the organic compounds on the particles like the glutaric acid from the ALS is not possible. Based on the EDS analysis it can be concluded that the Co-dopant consist below 0.5% by atomic ratio.

The following step was FTIR analysis of the obtained nanoparticles in the wavenumber range from 400 to 4,000 cm^{-1} . As can be seen in Fig. 4 the recorded spectrum reveals several peaks. The first peaks between 500–650 cm^{-1} can be ascribed to the vibrations in the metal oxides, including Fe–O and Co–O vibrations [68]. The peaks at 560 and 630 cm^{-1} can be identified as the Fe–O vibrations of the Fe_3O_4 crystal lattice [69,70]. The peak of about 600 cm^{-1} is broad and looks like an overlapping of two peaks, where the second peak at 570 cm^{-1} can be ascribed to the Co–O vibrations in the cobalt(II, III) oxides [71]. This band can be ascribed to the tetrahedral sites of Co, and the increase of the wavelength of about 400 can be ascribed to the octahedral sites, respectively [72,73]. It can also be attributed to the Co-Fe mixed oxide, confirming the Co doping in the iron oxide structure. The following range of 1,000–1,800 cm^{-1} reveals peaks that can be ascribed to the organic compounds that were incorporated into the nanoparticles

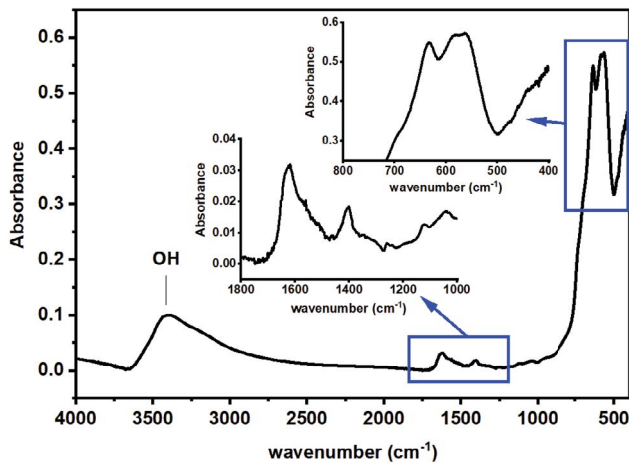


Fig. 4. Fourier-transform infrared spectrum for the obtained nanoparticles.

during synthesis from the ALS. The peaks from 1,000 to 1,400 cm^{-1} are characteristic of the C–O vibrations in carboxylic acid [69]. The peak of about 1,630 cm^{-1} is typical of the C=O bond [69]. The following broad peak between 3,000 and 350 cm^{-1} comes from the O–H groups that also correspond to the presence of carboxylic acid [74]. The presence of these peaks confirms the incorporation of the organic acids from ALS in the obtained material.

3.3. Magnetic and optical properties studies

The material obtained with co-precipitation was planned to be used for the magnetic separation of water pollutants and/or their photodegradation, so the magnetic properties were investigated. The measurements were performed in the range from –10 to 10 kOe. Fig. 5a presents the hysteresis curve with a narrow loop (see inset). Based on the shape of the magnetization curve, it can be concluded that the obtained nanoparticles have a superparamagnetic character. The magnetization saturation M_s is about 91 emu/g . The obtained M_s is similar to the values of iron-oxide-based nanoparticles [75,76]. The obtained results are promising for using the material in the magnetic separation of the compounds contaminating the water. The image in the curve presents the as-synthesized material that is collected on a magnet in distilled water. Then, the optical absorption spectra were recorded with UV-Vis spectrometry, Fig. 5b, where the optical band gap energy (E_g) of the prepared nanoparticles determined the transition of electrons from the valence band (VB) to the conduction band (CB) was estimated using the following formula:

$$\alpha h\nu = E(h\nu - E_g)^n \quad (2)$$

where α stands for the absorption coefficient of the material, K is the frequency-dependent material constant, and exponent n depends on the nature of transition in the semiconductor, that is, $n = 1/2$ for allowed direct transition [77].

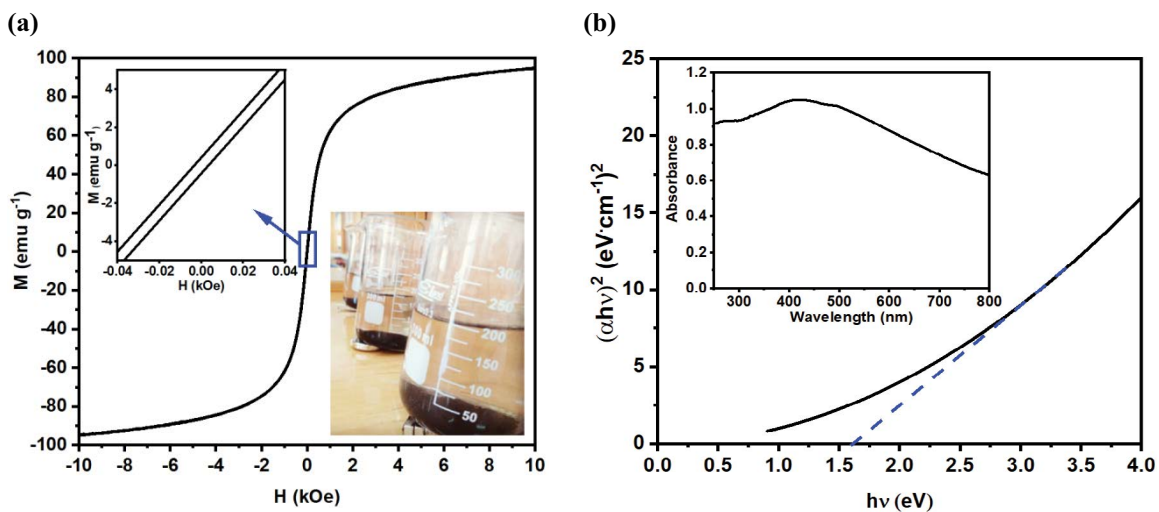


Fig. 5. (a) Magnetization curve of the obtained nanoparticles and (b) Tauc plot, where the inset shows the UV-Vis spectrum of nanoparticles' suspension in water.

Based on the spectrum, the Tauc plot was prepared (presented in the inset of Fig. 5b). Literature shows that the values for undoped Fe_3O_4 can vary depending on the size of nanoparticles from 11–40 nm [74,78]. The optical band gap value calculated in this work is about 1.6 eV, which is lower than the literature. At the same time, literature refers to the band gap for co-doped iron oxide as about 1.33–1.46 eV [79,80].

3.4. DFT studies

The DFT was applied to explore the spectral and electronic properties of tetracycline, in particular, the highest occupied molecular orbital (HOMO), lowest unoccupied molecular orbital (LUMO), molecular electrostatic potential (MEP), and natural bond orbital analysis (NBO) as well as molecule optimization. The dipole moment of tetracycline is 7.8549, while its total energy is $-1,563.51$ a.u. As can be seen in Fig. 6a the total electron density of TC indicates the electrophilic attract places. Fig. 6b and c shows the HOMO and LUMO of TC, respectively. Based on the presented images it is seen, where TC undergoes the adsorption.

Complementary, the molecular electrostatic potential was calculated using the following equation [81]:

$$V(r) = \sum_A \frac{Z_A}{|R_A - r|} - \int \frac{\rho(r') dr'}{|r' - r|} \quad (3)$$

where Z_A is a charge on nucleus A in the distance R_A , $\rho(r')$ denotes electronic density at the point r .

The MEP obtained enables the visualization of both, the charge distributions of tetracycline molecules and charge-related properties of tetracycline molecules. The MEP illustrates the electrophilic and nucleophilic attack reactivity, and negative (red color) and positive (blue color) regions, respectively. The negative regions are concentrated around H atoms, while the positive regions are concentrated around the O atoms with a double bond. The neutral region of the map is denoted by green color. In Fig. 6a the MEP surface of tetracycline was presented. The atom's color were marked according to the charges in the Mulliken type.

The frontier molecular orbitals (FMOs) of tetracycline are also considered. In Fig. 6b and c, the highest occupied molecular and lowest unoccupied molecular are presented. It turned out that the HOMO with orbital number 117 has a value of -0.2303 eV, while the LUMO with orbital number 118 has a value of -0.0344 eV. Having these two molecular orbitals one can calculate the energy gap, namely the HOMO-LUMO gap, which is considered an important stability index [82]. In turn, in the case of low energy HOMO nucleophiles are named hard nucleophiles [83], while the larger the energy gap, the harder molecule, which is connected with the stability of the molecule. In the case of tetracycline, the energy gap is quite low, that is, it is equal to 0.2647.

The electrostatic potential contour map for positive and negative potentials is shown in Fig. 7. The atom's color were marked according to the charges in the Mulliken type, similar to the molecular electrostatic potential.

To estimate the extent of internal charge transfers the NBO analysis was conducted. The natural Lewis structure description is 98.257% of the total electron density. Non-Lewis valance electrons are 1.753%, while non-Lewis Rydberg electrons are about 0.172% (the percent of the total non-Lewis electron is 1.580%). The selected second-order

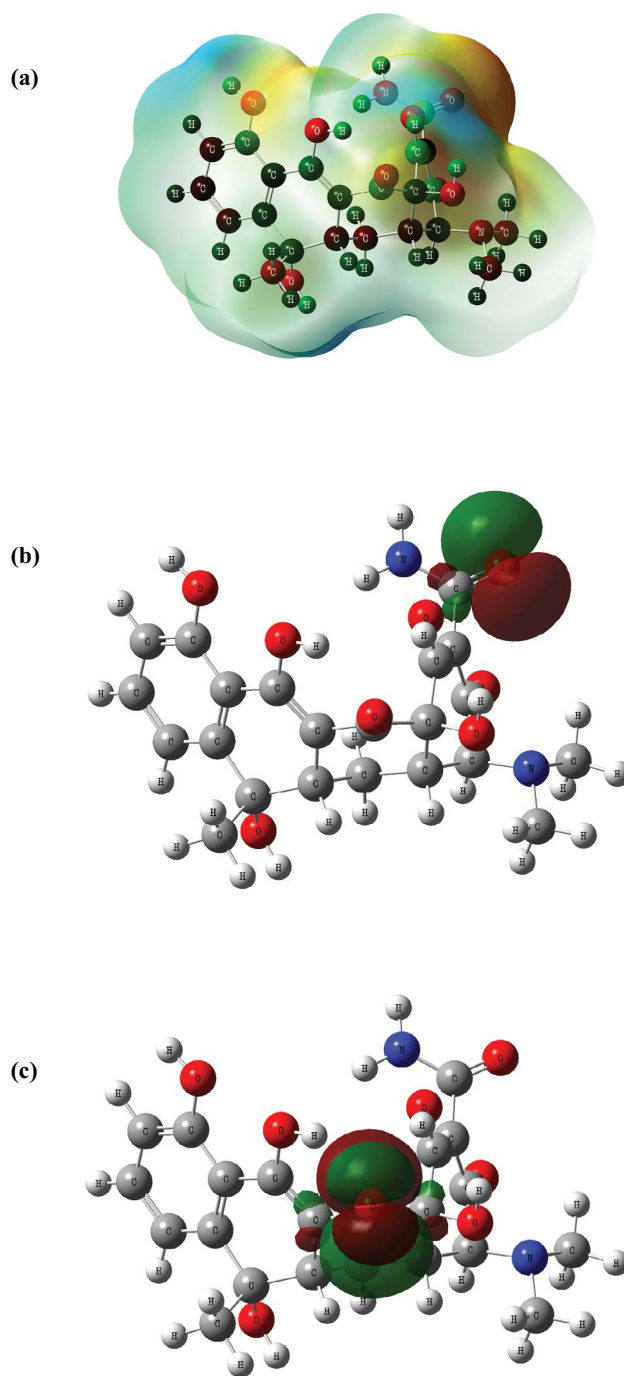


Fig. 6. (a) Total electron density isosurface is mapped with the molecular electrostatic potential of tetracycline, (b) the highest occupied molecular orbital of tetracycline, and (c) the lowest unoccupied molecular orbital of tetracycline.

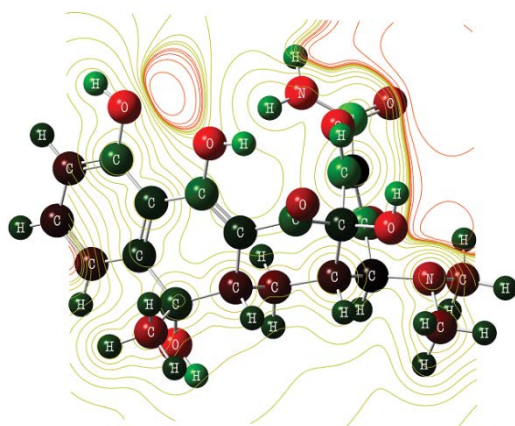


Fig. 7. Electrostatic potential contour of tetracycline.

perturbative estimates of donor–acceptor interactions are shown in Table 1. For each donor (i) and acceptor (j), the stabilization energy $E(2)$ is estimated with following formula:

$$E(2) = \Delta E_{ij} = q_i \frac{F(i,j)^2}{e_j - e_i} \quad (4)$$

where $F(i,j)$ denotes diagonal Fock matrix elements with the diagonal elements e_i and e_j and q_i is donor orbital occupancy. As the value of stabilization energy $E(2)$ increases, the intensity of the reaction between electron donors and electron acceptors increases, that is, propensity to donate electrons from electron donors to electron acceptors increases. The stabilization energy is proportional to the frequency of the hyperconjugation relations between electron donors and acceptors. The strongest interaction is for orbital NBO 74 localized on O_7 with the adjacent $RY^*(H_{56})$ bonds.

All numerical calculations have been prepared with Gaussian 09 software, and next, visualize with GaussView 5.0 [84]. The structure of the considered molecule was optimized using DFT with the commonly used exchange-correlation functional Becke-3-parameter-Lee-Yang-Parr (B3LYP) with the basis set with the default convergence criteria, without any constraint on the geometry, that is, with 6-23G**(d, p) [85–87]. The water was assumed as a solvent during numerical computations.

3.5. Photodegradation studies

Obtained nanoparticles were subsequently used as a photocatalyst degrading the tetracycline, one of the most common antibiotic-based aqueous pollutants [88]. Eq. (5) was used to calculate photodegradation efficiency.

$$\%H = \frac{(C_0 - C)}{C_0} \times 100\% \quad (5)$$

where: $\%H$ – photodegradation efficiency (%), C_0 – initial concentration of TC (here, 40 ppm), C – concentration of TC after a period of time t (ppm).

As can be seen in Fig. 8a, the absorbance of the 40 ppm TC solution decreases over time, where the 20 mL of TC solution was exposed on the 20 mg of magnetic particles were used. Complementary to the studies after the UV-Vis light exposition, the experiments without the light were performed. The measurements were performed at neutral pH. Therefore, the $\%H$ increasing in time shown in Fig. 8b refers to photodegradation. Use photocatalytic degradation to remove approx. 84.42% TC from the solution for 90 min, which corresponds to the C_t is about 6.23 ± 0.71 ppm from the initial 40 ppm of pollutant. That is much higher comparing to TC degradation itself [89]. Based on the experimental results obtained for the TC degradation with the iron oxide nanoparticles doped with cobalt, the effectiveness is similar to the results presented in the literature showing the promising properties of prepared material in the environmental studies [89–91]. Additionally, pH_{ZPC} was measured in 0.05 M and 0.1 M KNO_3 in different pH, where the initial pH ranged 4–12. The pH lower than 4 causes dissolution of nanoparticles, while in alkalic media over pH 12 the hydroxides form on the surface and particles can also dissolve. Therefore, more acidic and more alkalic conditions were not considered in measurement. Fig. 8c shows similar values in both solutions indicating the value of $pH_{ZPC} \sim 7.2$ –7.6. Obtained values are similar to the results presented in the literature, where the pH_{ZPC} is about 6.9 for $\gamma\text{-Fe}_2\text{O}_3$ [92], ~ 7 for Fe_3O_4 [93], and ~ 7 for Fe_2O_3 [89], 7–9 for ferrihydrites [54]. Then, the degradation of tetracycline was performed in pH 6–9 for 90 min. The results show the highest effectiveness of the process is in the pH 6–8 and the drop of about 30% is observed in pH 9. In pH 6 TC occurs in TCH_2 zwitterionic form and with the increase of pH it turns mono TCH^- and double TC^{2-} forms [94]. At alkali pH the surface of obtained particles is negatively charged and the drop of effectiveness is observed. It can be caused by electrostatic repulsion between negatively charged molecules of TC and the negatively charged surface of particles.

3.5.1. Photodegradation kinetics

The kinetic study of photodegradation molecules is very useful in predicting the removal rate and modelling this process. In this work tetracycline, photoassisted degradation by $Fe_3O_4@Co$ used linear models, first-order kinetic model, and second-order kinetics model which were described in Eqs. (6) and (7) [95]:

$$\ln\left(\frac{C_0}{C_t}\right) = k_1 t \quad (6)$$

$$tC_t^{-1} = \left(k_2 C_0^2\right)^{-1} + C_0^{-1} \quad (7)$$

where C_0 is the initial concentration of TC (ppm), C_t – concentration of tetracycline in time (ppm), t – time (min), k_1 is a photodegradation pseudo-first-rate constants (min^{-1}), k_2 stands for photodegradation pseudo-second-rate constant ($\text{g}/\text{min}\cdot\text{mg}$).

The experimental results are presented in Fig. 9 showing the linearity only for the $\ln(C_0/C_t)$ in the function of time. The coefficient f for the pseudo-first-order is equal to

Table 1

Stabilization energies ($E(2)$, in kcal/mol, Eq. (4)) between the selected orbitals obtained with the application of second-order perturbation theory analysis of Fock matrix elements in NBO analysis

Donor NBO (i)	Acceptor NBO (j)	$E(2)$	$E(j)-E(i)$	$F(i,j)$
		kcal/mol	a.u.	a.u.
BD (1)O 1 - C 14	RY*(1) C 14	0.67	1.77	0.031
BD (1)O 1 - H 41	RY*(1) C 14	2.03	1.66	0.052
BD (1)O 2 - C 16	RY*(1) C 16	0.60	1.79	0.029
BD (1)O 2 - H 42	BD*(1) C 16 - C 20	3.56	1.10	0.056
BD (1)O 3 - C 18	RY*(1) C 18	1.97	1.83	0.054
BD (2)O 3 - C 18	BD*(1) O 4 - H 50	1.37	0.80	0.030
BD (1)O 4 - C 19	BD*(1) C 11 - C 14	1.18	1.26	0.035
BD (1)O 4 - H 50	BD*(1) C 19 - C 23	4.38	1.42	0.071
BD (1)O 5 - C 22	BD*(1) C 12 - C 17	2.77	1.32	0.054
BD (1)O 5 - H 51	RY*(1) C 22	1.96	1.66	0.051
BD (1)O 6 - C 21	BD*(1) C 11 - C 15	0.66	1.43	0.028
BD (2)O 6 - C 21	BD*(1) N 9 - C 15	3.00	0.71	0.041
BD (1)O 7 - C 29	BD*(1) C 31 - C 32	1.57	1.51	0.044
BD (1)O 7 - H 56	RY*(1) C 29	1.97	1.65	0.051
BD (1)O 8 - C 30	BD*(1) N 10 - H 54	1.21	1.47	0.038
BD (2)O 8 - C 30	BD*(1) C 19 - C 23	0.85	1.01	0.026
BD (1)N 9 - C 15	RY*(3) C 27	0.57	1.30	0.025
BD (1)N 9 - C 15	RY*(1) C 28	0.75	1.51	0.030
BD (1)N 9 - C 27	RY*(2) C 28	0.54	1.57	0.026
BD (1)N 9 - C 28	RY*(1) C 27	0.71	1.46	0.029
BD (1)N 10 - C 30	BD*(1) O 8 - C 30	0.73	1.37	0.028
BD (1)N 10 - H 54	RY*(2) C 30	2.64	1.40	0.054
BD (1)N 10 - H 55	RY*(1) C 30	1.03	1.31	0.033
BD (1)C 11 - C 13	RY*(1) C 14	0.70	1.52	0.029
BD (1)C 11 - C 14	RY*(2) O 1	0.84	1.87	0.036
BD (1)C 11 - C 15	RY*(4) C 21	0.54	1.62	0.027
BD (1)C 11 - C 15	BD*(1) O 6 - C 21	2.40	1.16	0.047
BD (1)C 11 - H 33	BD*(1) O 1 - C 14	0.94	0.75	0.024
BD (1)C 11 - H 33	BD*(1) C 11 - C 15	0.86	0.87	0.024
BD (1)C 12 - C 13	BD*(1) C 13 - H 35	0.85	1.04	0.027
BD (1)C 12 - C 16	RY*(3) C 17	0.62	1.51	0.028
BD (1)C 12 - C 17	BD*(1) O 2 - C 16	1.95	0.88	0.037
BD (1)C 12 - C 17	BD*(1) O 3 - C 18	1.97	1.13	0.042
BD (1)C 12 - H 34	RY*(1) C 17	0.54	1.43	0.025
BD (1)C 13 - H 35	BD*(1) C 12 - C 17	2.76	0.91	0.045
BD (1)C 13 - H 36	RY*(1) C 12	0.74	1.54	0.030
BD (1)C 14 - C 18	BD*(1) C 11 - C 14	1.51	0.99	0.035
BD (1)C 14 - C 19	RY*(3) C 23	1.20	1.51	0.038
BD (1)C 14 - C 19	BD*(2) O 3 - C 18	3.56	0.65	0.044
BD (1)C 14 - C 19	BD*(1) C 11 - C 14	1.57	1.00	0.035
BD (1)C 15 - C 21	RY*(1) N 9	0.58	1.59	0.027
CR (1)O 1	RY*(1) C 14	2.61	19.88	0.204
CR (1)O 2	RY*(1) C 16	2.49	19.89	0.199
CR (1)O 3	BD*(1) C 14 - C 18	0.64	19.23	0.101
CR (1)O 4	RY*(1) C 19	2.62	19.87	0.204
CR (1)O 5	RY*(2) C 22	0.94	19.87	0.122
CR (1)O 6	BD*(1) C 21 - C 23	0.52	19.28	0.091
CR (1)O 7	RY*(1) C 29	2.27	19.87	0.190

Table 1 (Continued)

Table 1

Donor NBO (<i>i</i>)	Acceptor NBO (<i>j</i>)	<i>E</i> (2)	<i>E</i> (<i>j</i>)– <i>E</i> (<i>i</i>)	<i>F</i> (<i>i,j</i>)
		kcal/mol	a.u.	a.u.
CR (1) O 8	RY*(1) C 30	7.20	19.49	0.336
CR (1) N 9	RY*(3) C 28	1.23	14.75	0.120
CR (1) N 10	RY*(1) H 55	0.67	14.76	0.089
CR (1) C 11	RY*(2) C 13	1.00	10.83	0.093
CR (1) C 12	BD*(1) C 17 - C 22	0.79	10.69	0.083
CR (1) C 13	RY*(1) C 11	0.78	11.04	0.083
CR (1) C 32	BD*(1) C 26 - C 31	0.64	10.63	0.074
CR (1) C 32	BD*(1) C 31 - H 52	0.59	10.52	0.071
LP (1) O 1	RY*(1) C 14	3.76	1.51	0.068
LP (2) O 1	BD*(1) C 17 - C 18	0.73	0.73	0.021
LP (1) O 2	BD*(1) C 16 - C 25	1.68	0.92	0.035
LP (2) O 2	BD*(1) C 11 - C 13	0.50	0.64	0.016
LP (1) O 3	RY*(1) C 18	15.93	1.43	0.135
LP (2) O 3	BD*(1) C 17 - C 18	17.23	0.72	0.101
LP (1) O 4	RY*(1) C 19	3.46	1.46	0.064
LP (1) O 5	RY*(1) C 22	3.19	1.46	0.061
LP (2) O 5	BD*(2) C 17 - C 22	31.94	0.36	0.098
LP (1) O 6	RY*(1) C 21	15.72	1.42	0.134
LP (2) O 6	BD*(1) C 21 - C 23	20.57	0.68	0.106
LP (1) O 7	RY*(1) C 29	3.26	1.46	0.062
LP (2) O 7	BD*(2) C 24 - C 29	31.90	0.32	0.099
LP (1) O 8	RY*(1) C 30	15.32	1.31	0.127
BD*(2) O 3 - C 18	RY*(2) O 3	0.56	1.20	0.088
BD*(2) O 6 - C 21	BD*(1) N 9 - C 15	1.10	0.35	0.059
BD*(2) O 8 - C 30	RY*(2) O 8	1.33	1.03	0.090
BD*(2) C 17 - C 22	RY*(1) C 17	0.59	0.88	0.058

0.9902, while for the pseudo-second-order non-linear trend is observed and *f* is 0.8929. Compared to the factors obtained in the data the photodegradation of TC could be described as pseudo-first-order. The result is similar to the kinetics presented in the literature [96]. Table 2 compares different materials proposed to photo-assisted degradation of TC, whereas variables such as effectiveness, time, the dose of adsorbent attitude to volume, and kinetic orders.

Based on the experimental results obtained in this work the photodegradation undergoes the pseudo-first-order kinetics which is in a good agreement with the data presented in the literature for iron-oxide based nanomaterials and the other semiconducting nanostructures. The contact time about 90 min leads to the effective treatment reaching 84.42% effectiveness.

3.5.2. Reusability studies, operation in H₂O₂, and proposed mechanism of photodegradation

As the economical aspect of nanomaterials application is an important issue, the reusability of particles was studied as follows. After the first cycle, nanoparticles were separated with magnet from the TC post-treated solution and placed in the separate beaker, where they were sonicated for 5 min in distilled water, then for 5 min in methanol, and

continuously in distilled water also for 5 min. Then, fresh TC was prepared and the TC concentration was adjusted to the initial value and exposed on the nanoparticles for 90 min under the UV-Vis irradiation. The photocatalyst was studied for five cycles of operation in pH 7. After the treatment photocatalyst was centrifuged and collected from the reaction mixture. Fig. 10a shows that the performance efficiency was not reduced significantly. It is important to highlight that the Co was not released from the nanoparticles.

Following studies were performed in different experimental conditions, in particular in presence of 3% solution of H₂O₂, 0.01 M H₂SO₄, and 0.01 M HNO₃ to compare the effectiveness of TC degradation in neutral pH. Measurements were performed for the same dosage of adsorbent like described above. Despite the application of strong acids, the degradation of TC under UV-Vis irradiation is relatively low comparing to the operation in water. This effect can be caused by the surface degradation of nanoparticles in the acidic media, especially when it comes to solutions with pH lower than 4. Likewise expected, the highest effectiveness of about ~92.2% was recorded for H₂O₂ solution. Such effect is caused by the generation of radicals that have an oxidative properties and high reactivity [105,106].

Next, the flab band potential was determined using Mott–Schottky analysis using electrochemical impedance

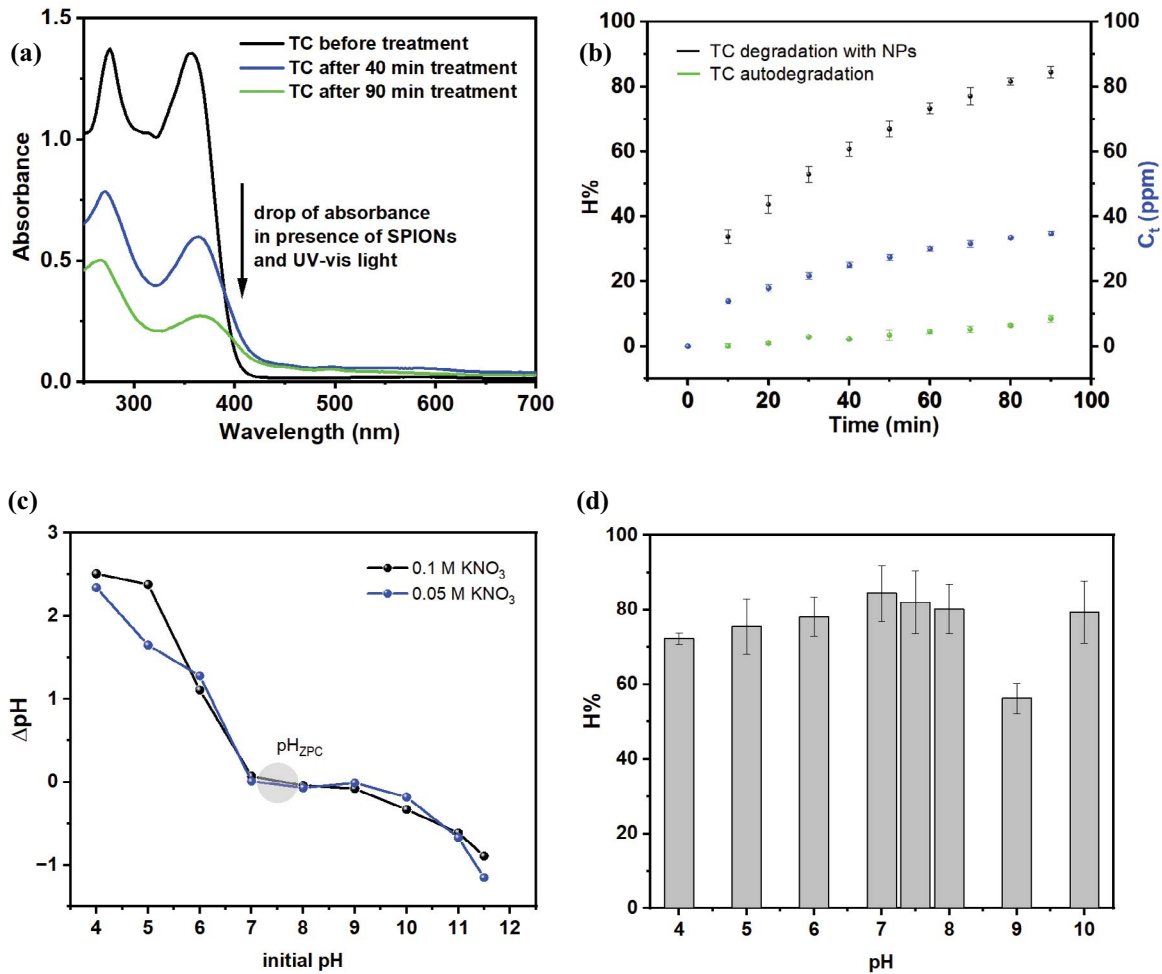


Fig. 8. (a) UV-Vis spectra of 40 ppm tetracycline before and after treatment of magnetic nanoparticles, (b) $H\%$ after the treatment, and (c) pH_{pzc} of obtained material.

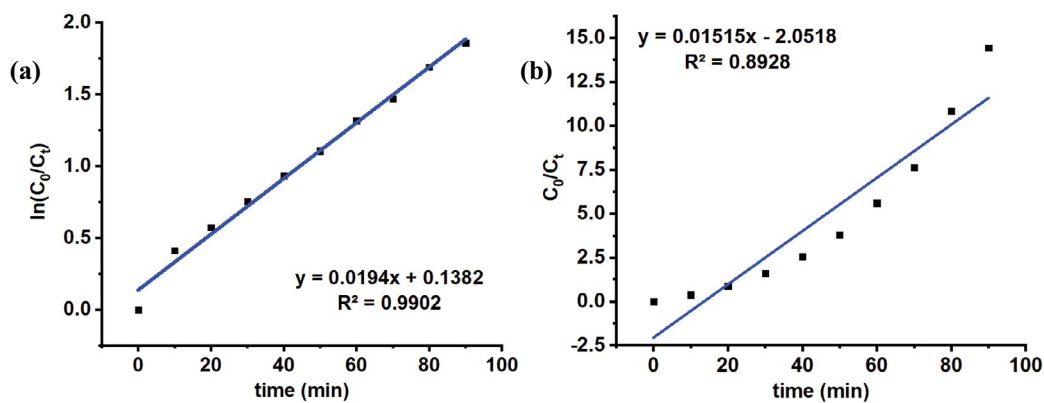


Fig. 9. (a) Linear fitting of the experimental results on the (initial concentration 40 ppm) tetracycline removal to the pseudo-first-order model and (b) pseudo-second-order model.

spectroscopy (EIS) at 100 kHz. Measurements were performed in three electrode system using glassy carbon electrode 3 mm diameter (0.72 cm²) vs. reference electrode Ag|AgCl|KCl (saturated), and Pt wire as a counter electrode

in 0.1 M KCl using BioLogic electrochemical setup. The flat band potential extrapolated from the curve is -0.18 V (-4.36 eV) vs. SHE. Based on the Tauc plot where the band gap energy was about 1.6 eV the edge of the valence band

Table 2
Photodegradation effectiveness of tetracycline

Adsorbent	H%, contact time	C ₀ of tetracycline, mass of adsorbent (<i>m_{ads}</i>), adsorption kinetics	References
TiO ₂ , 5P-TiO ₂ , 12.5P-TiO ₂ , and 20P-TiO ₂	H% = 58.02%, 85.50%, 99.16%, 85.49% and 85.52%, <i>t</i> = 40.39 min	C ₀ = 29.93 ppm, <i>m_{ads}</i> = 1 g/L, quasi-first-order kinetics	[97]
Sr _{0.05} Fe _{1.95} O ₃	H% = 85%, <i>t</i> = 60 min	C ₀ = 20 mg/L, <i>m_{ads}</i> = 30 μg/mL, <i>V</i> = 1 L, pseudo-first-order kinetics	[98]
CdS nanoparticles	H% = 80%, <i>t</i> = 60 min	C ₀ = 83 μM, <i>m_{ads}</i> = 10 mg/40 mL, first-order kinetics	[99]
10%-NiFe ₂ O ₄ /g-C ₃ N ₄	H% = 94.5%, <i>t</i> = 80 min	Data	[100]
CeO ₂ /CBOC	H% = 79.50%, <i>t</i> = 90 min	C ₀ = 20 mg/L, <i>m_{ads}</i> = 35 mg, pseudo-first-order kinetics	[101]
Ce (4 mol%)-CuO	H% = 83%, <i>t</i> = 30 min, with H ₂ O ₂ ; H% = 25%, <i>t</i> = 30 min, without H ₂ O ₂	C ₀ = 10 mg/L, <i>m_{ads}</i> = 10 mg/50 mL, pseudo-second-order kinetics	[102]
Fe ₃ O ₄	H% = 40%, <i>t</i> = 60 min	C ₀ = 83 μM, <i>m_{ads}</i> = 10 mg/10 mL	[103]
ZnO and ZnO/γ-Fe ₂ O ₃ composite	H% = 68.28% and 88.52% <i>t</i> = 210 min	C ₀ = 30 ppm, <i>m_{ads}</i> = 15 mg/20 mL, first-order kinetics	[104]
Fe ₃ O ₄ -doped with Co from acid leaching solution	H% = 84.42%, <i>t</i> = 90 min	C ₀ = 40 ppm, <i>m_{ads}</i> = 10 mg/10 mL, pseudo-first-order kinetic order	This work

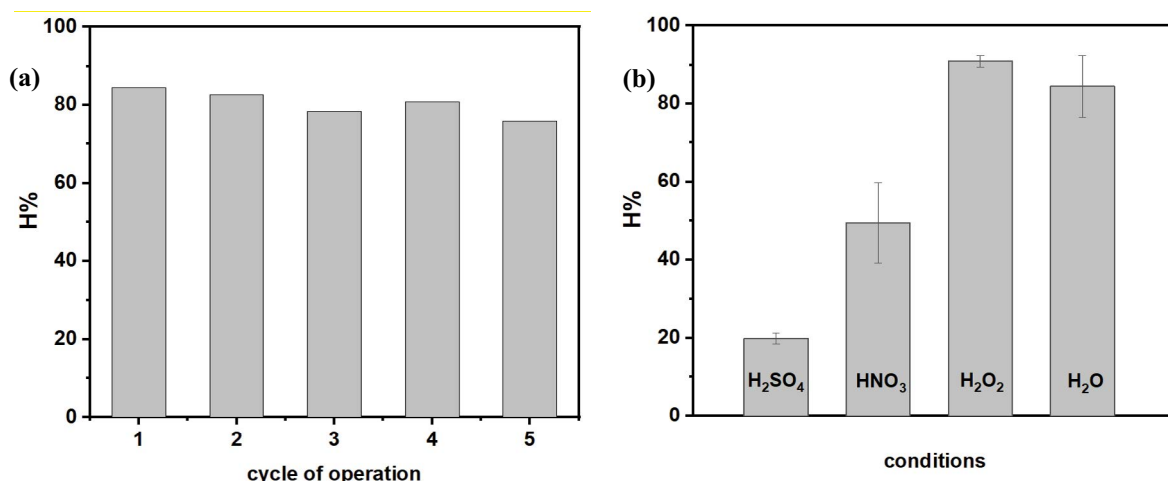
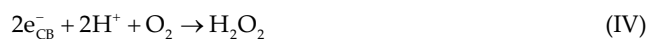
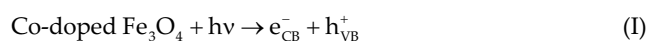


Fig. 10. (a) H% change with five cycles of operation and (b) in various conditions, in particular H₂SO₄, HNO₃, and H₂O₂.

can be estimated around -5.96 eV. Positive slope of the obtained Mott–Schottky plot suggests *n*-type semiconductor, Fig. 11. Comparing to the energy diagram for bare iron oxide-based nanoparticles [54], the position of CB and VB for obtained co-doped nanoparticles is a bit lower in eV scale [107,108].

Formation of H₂O₂ through the excitations of electrons from valence band (VB) to conduction band (CB) can trigger photo-Fenton reaction [109,110]. The proposed mechanism of TC degradation can undergo two pathways. First, holes and electrons are generated in the co-doped particles (1) and then, holes react in the valence band with the particular molecules (2) and (3), where the most probable for the oxidation of adsorbed OH⁻ ions with holes (3). Electrons in conduction band also react within reactions (4) and (5) [111,112].

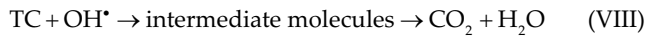


Besides reactions (2)–(5) the reduction of Fe³⁺ ions (6) and oxidation of Fe²⁺ ions in the co-doped iron oxide can appear (7):





Due to the high reactivity of radicals, they can lead to the degradation of TC (8).



Second mechanism is related directly with the H_2O_2 formation, where the reactive molecules through oxidation/reduction of iron ions occur, in particular Fenton (9) and photo-Fenton (10) reactions [113,114].



Based on the band structure of iron oxide type of nanoparticles and the Tauc plot and Mott–Schottky plot the

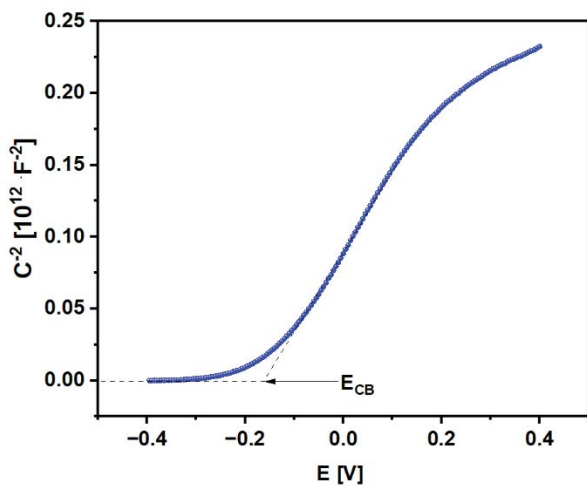


Fig. 11. Mott–Schottky plot for obtained nanoparticles.

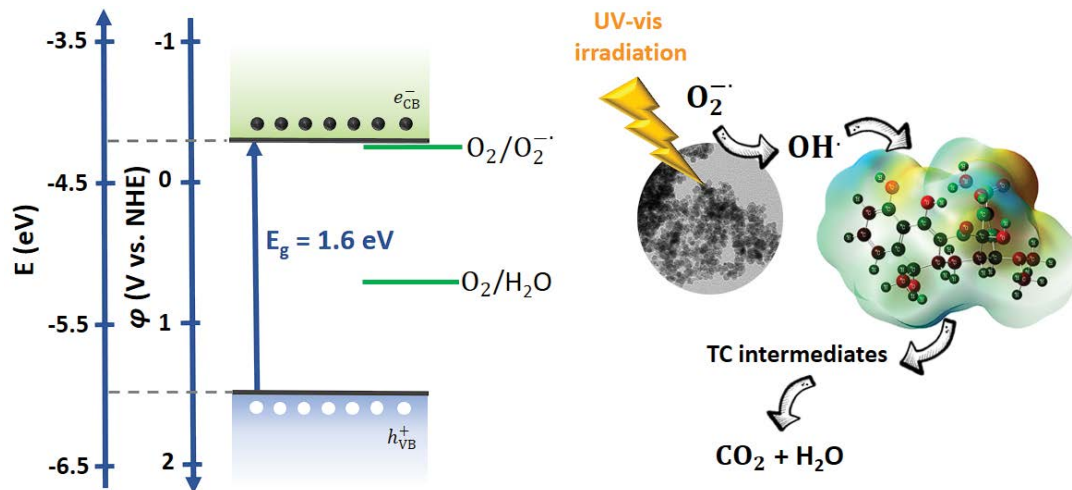


Fig. 12. Scheme of energetic diagram of obtained nanoparticles and mechanism on photocatalytic degradation of tetracycline.

proposed mechanism is drawn in Fig. 12. Obtained results are similar to the literature [115], where generated carriers play a crucial role in the TC degradation.

4. Discussion

Spent lithium-ion batteries are the source of many valuable metals, which achieve even higher metal content than their natural counterparts [116]. The recovery of raw materials from waste batteries has not only an economic basis related to the running out of natural resources but also an ecological basis related to environmental pollution and a negative impact on human health [117]. The most economically efficient is recycling the LiBs cathodes [33]. The leaching process plays a crucial role in hydrometallurgical recycling. Inorganic acids are efficient and fast-acting, while characterized by poor selectivity, which translates into leaching metallic impurities into the leaching solution [118]. The commonly used inorganic acids are hydrochloric acid (HCl), phosphoric acid (H_3PO_4), sulfuric acid (H_2SO_4), and nitric acid (HNO_3) [116]. The organic acids enable selective separation of impurities, while they entail high economic costs in the case of large-scale recycling processes. In turn, the alkaline leaching provides the ammonia selectivity and retrievability characteristic [119]. By adding reducing agents, for example, hydrogen peroxide (H_2O_2), the optimization of the metals recovery is possible [120], while ascorbic acid may contribute to more efficient cobalt recovery due to the fact that enables the conversion of Co(III) to Co(II) [23]. The inorganic acids are characterized by strong acidity and may produce a large amount of poisonous and acidic waste gas, for example, Cl_2 , NO_x , SO_x [121]. Thus, acid/alkaline leaching is effective but requires the disposal of costly waste, which contributes to the total cost recovery of the entire process. As one of the examples of supporting the leaching process in the interests of the environment and human health, preliminary research on the use of ultrasound [122], microwaves [123,124], or selective leaching [125] is being carried out. Future directions of LiBs recycling development should include the development of green solvents that will replace traditional acid/base leaching solutions as well as the scaling

up of the process. Another interesting solution to increase the efficiency of LiBs recycling is connected with the application of artificial intelligence (AI) [126]. Ruhatiya et al. [127] neural networks were used to optimize the bioleaching process to provide maximal metal recovery.

Magnetic particles are considered an efficient tool for the remediation of wastewater [128,129]. The main issues connected with the application of magnetic particles in environmental studies are their stability and reusability, which are associated with the type of admixture [130]. Das et al. [42] polydopamine was applied to improve the stability of magnetic nanoparticles Fe_3O_4 @PDA-ZIF-8. Also, other properties of magnetic nanoparticles depend on the components from which they were obtained. The magnetic banana leaf sheath carbon-Fresh is characterized by higher magnetism saturation and higher pseudo-first-order rate in comparison to the magnetic banana leaf sheath carbon-dry [131]. Another factor, which influences the removal or degradation efficiency is pH, while the surface charges vary at different pH [132]. Zhang et al. [133] was shown that magnetic nanoparticles doped with polydopamine polymer are able to effectively remove heavy metal ions and organic dyes, namely, methylene blue and tartrazine, from water. The experimental research by the study of Chen et al. [134] indicated that iron oxide-based magnetic particles demonstrated very rapid absorption of the Cr(IV) and Ni(II), while the Ni(II) removal is more efficient in the acidic range. The removal efficiency of both heavy metal ions increases with increasing process temperature. The iron oxide-based sulfonated magnetic nanoparticles were also successfully applied to remove cadmium and lead ions from water [51]. In turn, magnetic SnO_2 nanoparticles were used for the photodegradation of indigo carmine dye under a UV-Vis lamp [135].

The growing necessity to purify water from various harmful substances forces the need to improve the existing methods [136]. Preliminary laboratory tests presented above confirm that magnetic particles can effectively remove or degrade various types of harmful substances, including pharmaceutical-origin chemical compounds, heavy metal ions, and dyes. In this paper, we concentrate on counteracting the effects of the release of antibiotics into aquatic environments, in particular, eco-toxic tetracycline, which is released into the water and causes the rapid development of bacterial resistance. The polydopamine increases tetracycline adsorption capacity in the case of Fe_3O_4 @PDA-ZIF-8 [42]. Karimi and Namazi [136] for the absorption of the tetracycline and amoxicillin the Fe_3O_4 @maltose-functionalized triazine dendrimer in alginate ($\text{Alg}/\text{Fe}_3\text{O}_4$ @C@TD) was proposed. The nanocomposite based on microbial cellulose (MC@nano-) can absorb 48.0% of tetracycline, that is, 50 mg of tetracycline after 120 min, by extending the time to 180 min efficiency increased to approx. 97.0% [137]. However, the extension of the process duration entails an increase in economic costs. Thus, the iron oxide nanoparticles doped with active carbon enable tetracycline degradation [138]. The $\text{CuCoFe}_2\text{O}_4$ @Chitosan (Ch) adsorbent provides tetracycline removal with an efficiency of 82.16% after four adsorption–desorption cycles [139]. Zhu et al. [140] the magnetic nanoparticles of doped biochar were applied to the degradation of tetracycline with the efficiency of 99.0% after 24 min. Similar efficiency is ensured

by $\text{S-ZnFe}_2\text{O}_4$ [141]. Kumar et al. [142] it was suggested that including electron donors provide an increase in H_2O_2 production and tetracycline degradation rates in the case of $\text{Ag/s-(Co}_3\text{O}_4/\text{NiFe}_2\text{O}_4)$.

In Table 1, the photodegradation effectiveness of tetracycline in the case of various magnetic nanoparticle-based materials taking into account contact time, the mass of adsorbent, and adsorption kinetics were made. It turned out that the results presented in our work are promising, offering the fast and effective treatment of TC maintaining the magnetic separation of the material from the solution. The superparamagnetic iron oxide (Fe_3O_4) nanoparticles were produced based on battery waste and applied to the degradation of the tetracycline. It turned out that the optimal tetracycline effectiveness was approx. 84.42% with 90 min of process duration, and 40 ppm of initial TC concentration. The results obtained suggest that the application of battery waste-derived superparamagnetic iron oxide (Fe_3O_4) nanoparticles can be considered a low-cost and environmentally friendly solution for removal of the antibiotic contaminants, in particular, tetracycline in water treatment processes.

5. Conclusions

This work presents the application of the acid-leaching solution to dope magnetic nanoparticles with cobalt. The ALS was used as a source of Co(II) ions during wet co-precipitation synthesis of the superparamagnetic iron oxide nanoparticles. The UV-Vis spectrometry confirmed the removal of Co^{2+} ions from the solution after synthesis. The nanostructural particles are sized approx. 15.0 ± 4.80 nm in diameter and the band gap of about 1.6 eV reveal the superparamagnetic particles with the M_s approx. 91 emu/g offering fast, simple, and cost-effective treatment of aqueous contaminants. UV-Vis spectra of the ALS bath before and after the use confirm the removal of Co^{2+} ions from the bath after synthesizing SPIONs. EDS mapping revealed the uniform distribution of Co in the whole sample, and the XRD shows the spinel structure that can be ascribed to the iron oxide-based material. The flat band potential of about -0.18 V vs. SHE was estimated using Mott–Schottky plot. The position of the edges of conduction band and valence band are in the range where the formation of radicals under the irradiation appears improving the effectiveness of the TC degradation. The TC elimination efficiency was approximately 84.42% for neutral pH without additional compounds, while the effectiveness is reduced under the application of strong oxidative acids like H_2SO_4 and HNO_3 . Application of H_2O_2 improves the TC degradation for the generation of reactive radicals in the solution during irradiation. To sum up, we demonstrated effective, simple, and economical removal of Co from ALS as an effective way to deal with secondary battery waste though the formation of functional nanoparticles occurring photocatalytic properties. Proposed material has a potential in environmental studies in the broad pH range from 4 to 10 and it offers facile surface recovery and reuse.

Symbols

D	—	Crystallite size, nm
B	—	Full width-at-half-maximum length of the reflection

θ	—	Bragg angle, °
λ	—	X-ray wavelength, nm
k	—	Dimensionless shape factor
E_g	—	Optical band gap energy, eV
V_B	—	Valence band, eV
CB	—	Conduction band, eV
α	—	Absorption coefficient of the material
K	—	Frequency-independent material constant
$V(r)$	—	Molecular electrostatic potential
ZA	—	Charge on nucleus A in the distance RA
$r(r')$	—	Electronic density at the point r
$E(2)$	—	Stabilization energy, kcal/mol
(i)	—	Donor
(j)	—	Acceptor
$F(i,j)$	—	Diagonal Fock matrix elements with the diagonal elements e_i and e_j , a.u.
q_i	—	Donor orbital occupancy
%H	—	Photodegradation efficiency
C_0	—	Initial concentration of TC, ppm
C	—	Concentration of TC after a period of time t , ppm
M_s	—	Saturation magnetization, emu/g
t	—	Time, min
TC	—	Tetracycline
k_1	—	Photodegradation pseudo-first-rate constants, min^{-1}
k_2	—	Photodegradation pseudo-second-rate constant, $\text{g}/\text{min}\cdot\text{mg}$
SHE	—	Saturated hydrogen electrode

References

- [1] A. Porvali, M. Aaltonen, S. Ojanen, O. Velázquez-Martínez, E. Eronen, F. Liu, B.P. Wilson, R. Serna-Guerrero, M. Lundström, Mechanical and hydrometallurgical processes in HCl media for the recycling of valuable metals from Li-ion battery waste, *Resour. Conserv. Recycl.*, 142 (2019) 257–266.
- [2] S.-j. Gao, W.-f. Liu, D.-j. Fu, X.-g. Liu, Research progress on recovering the components of spent Li-ion batteries, *New Carbon Mater.*, 37 (2022) 435–460.
- [3] C. Peng, J. Hamuyuni, B.P. Wilson, M. Lundström, Selective reductive leaching of cobalt and lithium from industrially crushed waste Li-ion batteries in sulfuric acid system, *Waste Manage.*, 76 (2018) 582–590.
- [4] J. Wang, Y. Zhang, L. Yu, K. Cui, T. Fu, H. Mao, Effective separation and recovery of valuable metals from waste Ni-based batteries: a comprehensive review, *Chem. Eng. J.*, 430 (2022) 135767, doi: 10.1016/j.cej.2022.135767.
- [5] W. Mroziak, M.A. Rajaeifar, O. Heidrich, P. Christensen, Environmental impacts, pollution sources and pathways of spent lithium-ion batteries, *Energy Environ. Sci.*, 14 (2021) 6099–6121.
- [6] G. Mishra, R. Jha, A. Meshram, K.K. Singh, A review on recycling of lithium-ion batteries to recover critical metals, *J. Environ. Chem. Eng.*, 10 (2022) 108534, doi: 10.1016/j.jece.2022.108534.
- [7] A. Pražanová, V. Knap, D.-I. Stroe, Literature review, recycling of lithium-ion batteries from electric vehicles, Part I: recycling technology, *Energies*, 15 (2022) 1086, doi: 10.3390/en15031086.
- [8] O. Velázquez-Martínez, J. Valio, A. Santasalo-Aarnio, M. Reuter, R. Serna-Guerrero, A critical review of lithium-ion battery recycling processes from a circular economy perspective, *Batteries*, 5 (2019) 68, doi: 10.3390/batteries5040068.
- [9] M. Chen, X. Ma, B. Chen, R. Arsenault, P. Karlson, N. Simon, Y. Wang, Recycling end-of-life electric vehicle lithium-ion batteries, *Joule*, 3 (2019) 2622, doi: 10.1016/j.joule.2019.09.014.
- [10] N. Bolan, S.A. Hoang, M. Tanveer, L. Wang, S. Bolan, P. Sooriyakumar, B. Robinson, H. Wijesekara, M. Wijesooriya, S. Keerthanan, M. Vithanage, B. Markert, S. Fränzle, S. Wünschmann, B. Sarkar, A. Vinu, M.B. Kirkham, K.H.M. Siddique, J. Rinklebe, *From mine to mind and mobiles – lithium contamination and its risk management*, *Environ. Pollut.*, 290 (2021) 118067, doi: 10.1016/j.envpol.2021.118067.
- [11] D. Lisbona, T. Snee, A review of hazards associated with primary lithium and lithium-ion batteries, *Process Saf. Environ. Prot.*, 89 (2011) 434–442.
- [12] S. Rarotra, S. Sahu, P. Kumar, K.H. Kim, Y.F. Tsang, V. Kumar, P. Kumar, M. Srinivasan, A. Veksha, G. Lisak, Progress and challenges on battery waste management: a critical review, *Chemistry*, 5 (2020) 6182–6193.
- [13] F. Thibon, M. Metian, F.O. Oberhänsli, M. Montanes, E. Vassileva, A.M. Orani, P. Telouk, P. Swarzenski, N. Vigier, Bioaccumulation of lithium isotopes in mussel soft tissues and implications for coastal environments, *ACS Earth Space Chem.*, 5 (2021) 1407–1417.
- [14] A.T. Chow, Proactive approach to minimize lithium pollution, *J. Environ. Qual.*, 51 (2022) 872–876.
- [15] Y. Bai, N. Muralidharan, Y.K. Sun, S. Passerini, M. Stanley Whittingham, I. Belharouak, Energy and environmental aspects in recycling lithium-ion batteries: concept of battery identity global passport, *Mater. Today*, 41 (2020) 304.
- [16] R.K. Rai, S.S. Lee, M. Zhang, Y.F. Tsang, K.H. Kim, Heavy metals in food crops: health risks, fate, mechanisms, and management, *Environ. Int.*, 125 (2019) 365–385.
- [17] E.M. Melchor-Martínez, R. Macías-Garbett, A. Malacara-Becerra, M.N.H. Iqbal, J.E. Sosa-Hernández, R. Parra-Saldívar, Environmental impact of emerging contaminants from battery waste: a mini review, *Case Stud. Chem. Environ. Eng.*, 3 (2021) 100104, doi: 10.1016/j.csee.2021.100104.
- [18] X. Zhu, J. Xiao, Q. Mao, Z. Zhang, Z. You, L. Tang, Q. Zhong, A promising regeneration of waste carbon residue from spent lithium-ion batteries via low-temperature fluorination roasting and water leaching, *Chem. Eng. J.*, 430 (2022) 132703, doi: 10.1016/j.cej.2021.132703.
- [19] F. Larouche, F. Tedjar, K. Amouzegar, G. Houlachi, P. Bouchard, G.P. Demopoulos, K. Zaghbi, Progress and status of hydrometallurgical and direct recycling of Li-ion batteries and beyond, *Materials*, 13 (2020) 801, doi: 10.3390/ma13030801.
- [20] P. Meshram, B.D. Pandey, T.R. Mankhand, Recovery of valuable metals from cathodic active material of spent lithium-ion batteries: leaching and kinetic aspects, *Waste Manage.*, 45 (2015) 306–313.
- [21] W. Urbańska, Recovery of Co, Li, and Ni from spent Li-ion batteries by the inorganic and/or organic reducer assisted leaching method, *Minerals*, 10 (2020) 555, doi: 10.3390/min10060555.
- [22] W. Urbańska, M. Osial, Investigation of the physico-chemical properties of the products obtained after mixed organic-inorganic leaching of spent Li-ion batteries, *Energies*, 13 (2020) 6732, doi: 10.3390/en13246732.
- [23] R. Golmohammadzadeh, F. Faraji, F. Rashchi, Recovery of lithium and cobalt from spent lithium-ion batteries (LiBs) using organic acids as leaching reagents: a review, *Resour. Conserv. Recycl.*, 136 (2018) 418–435.
- [24] A. Benedetto Mas, S. Fiore, S. Fiorilli, F. Smeacetto, M. Santarelli, I. Schiavi, Analysis of lanthanum and cobalt leaching aimed at effective recycling strategies of solid oxide cells, *Sustainability*, 14 (2022) 3335, doi: 10.3390/su14063335.
- [25] X. Chen, H. Huang, L. Pan, T. Liu, M. Niederberger, Fully integrated design of a stretchable solid-state lithium-ion full battery, *Adv. Mater.*, 31 (2019) 1904648, doi: 10.1002/adma.201904648.
- [26] G. Zhang, X. Yuan, Y. He, H. Wang, W. Xie, T. Zhang, Organics removal combined with in situ thermal-reduction for enhancing the liberation and metallurgy efficiency of LiCoO₂ derived from spent lithium-ion batteries, *Waste Manage.*, 115 (2020) 113–120.
- [27] Y. Wang, Z. Xu, X. Zhang, E. Yang, T. Yanan, A green process to recover valuable metals from the spent ternary lithium-ion batteries, *Sep. Purif. Technol.*, 299 (2022) 121782, doi: 10.1016/j.seppur.2022.121782.

- [28] M. Baniasadi, F. Vakilchah, N. Bahaloo-Horeh, S.N. Mousavi, S. Farnaud, Advances in bioleaching as a sustainable method for metal recovery from e-waste: a review, *J. Ind. Eng. Chem.*, 76 (2019) 75–90.
- [29] J.J. Roy, B. Cao, S. Madhavi, A review on the recycling of spent lithium-ion batteries (LiBs) by the bioleaching approach, *Chemosphere*, 282 (2021) 130944, doi: 10.1016/j.chemosphere.2021.130944.
- [30] P. Xu, Q. Dai, H. Gao, H. Liu, M. Zhang, M. Li, Y. Chen, K. An, Y.S. Meng, P. Liu, Y. Li, S.J. Spangenberg, L. Gaines, J. Lu, Z. Chen, Efficient direct recycling of lithium-ion battery cathodes by targeted healing, *Joule*, 4 (2020) 2609–2626.
- [31] Y. Zhao, O. Pohl, A.I. Bhatt, G.E. Collis, P.J. Mahon, T. R  ther, A.F. Hollenkamp, A review on battery market trends, second-life reuse, and recycling, *Sustainable Chem.*, 2 (2021) 167–205.
- [32] L. Olsson, S. Fallahi, M. Schnurr, D. Diener, P. Van Loon, Circular business models for extended EV battery life, *Batteries*, 4 (2018) 57, doi: 10.3390/batteries4040057.
- [33] J.J. Roy, S. Rarotra, V. Krikstolaityte, K.W. Zhuoran, Y.D.-I. Cindy, X.Y. Tan, M. Carboni, D. Meyer, Q. Yan, M. Srinivasan, Green recycling methods to treat lithium-ion batteries e-waste: a circular approach to sustainability, *Adv. Mater.*, 34 (2022) 2103346, doi: 10.1002/adma.202103346.
- [34] A. De, Nanomaterial synthesis from end-of-cycle products: a sustainable way of waste valorisation, *ChemBioEng Rev.*, 9 (2022) 337–350.
- [35] K.K. Brar, S. Magdoui, A. Othmani, J. Ghanei, V. Narisetty, R. Sindhu, P. Binod, A. Pugazhendhi, M.K. Awasthi, A. Pandey, Green route for recycling of low-cost waste resources for the biosynthesis of nanoparticles (NPs) and nanomaterials (NMs)-a review, *Environ. Res.*, 207 (2022) 112202, doi: 10.1016/j.envres.2021.112202.
- [36] H. Hao, G. Liu, Y. Wang, B. Shi, K. Han, Y. Zhuang, Y. Kong, Simultaneous cationic Cu(II)-anionic Sb(III) removal by $\text{NH}_2\text{-Fe}_3\text{O}_4\text{-NTA}$ core-shell magnetic nanoparticle sorbents synthesized via a facile one-pot approach, *J. Hazard. Mater.*, 362 (2019) 246–257.
- [37] M. Rouhani, S.D. Ashrafi, K. Taghavi, M. Naimi Joubani, J. Jaafari, Evaluation of tetracycline removal by adsorption method using magnetic iron oxide nanoparticles (Fe_3O_4) and clinoptilolite from aqueous solutions, *J. Mol. Liq.*, 356 (2022) 119040, doi: 10.1016/j.molliq.2022.119040.
- [38] C. Capan, A.-E. Segneanu, O. Grad, M. Mihailescu, M. Capan, I. Grozescu, Assessment of the different type of materials used for removing phosphorus from wastewater, *Materials*, 14 (2021) 4371, doi: 10.3390/ma14164371.
- [39] S. Wei, R. Kamali, Trifunctional mesoporous magnetic adsorbent-photocatalyst nanocomposite for efficient removal of potassium ethyl xanthate from mining wastewater, *J. Water Process. Eng.*, 49 (2022) 103067, doi: 10.1016/j.jwpe.2022.103067.
- [40] S. Wei, A. Kamali, Waste plastic derived $\text{Co}_3\text{Fe}_2/\text{CoFe}_2\text{O}_4$ @carbon magnetic nanostructures for efficient dye adsorption, *J. Alloys Compd.*, 886 (2021) 161201, doi: 10.1016/j.jallcom.2021.161201.
- [41] A. Dehghan, A. Zarei, J. Jaafari, M. Shams, A. Mousavi Khaneghah, Tetracycline removal from aqueous solutions using zeolitic imidazolate frameworks with different morphologies: a mathematical modeling, *Chemosphere*, 217 (2019) 250–260.
- [42] C. Das, S. Singh, S. Bhakta, P. Mishra, G. Biswas, Bio-modified magnetic nanoparticles with *Terminalia arjuna* bark extract for the removal of methylene blue and lead(II) from simulated wastewater, *Chemosphere*, 291 (2022) 132673, doi: 10.1016/j.chemosphere.2021.132673.
- [43] L.B. Beltran, A.C. Ribeiro, E. da Costa Neves Fernandes de Almeida Duarte, R. Bergamasco, A. Marquetotti Salcedo Vieira, Green Magnetic Nanoparticles in Industrial Wastewater Treatment: An Overview, T. Karchiyappan, R.R. Karri, M.H. Dehghani, Eds., *Industrial Wastewater Treatment*, Springer, Cham, 2022, pp. 187–207.
- [44] J. Barasarathi, P.S. Abdullah, E.C. Uche, Application of magnetic carbon nanocomposite from agro-waste for the removal of pollutants from water and wastewater, *Chemosphere*, 305 (2022) 135384, doi: 10.1016/j.chemosphere.2022.135384.
- [45] I.J. Sahib, L.S. Jasim, A.F. Alkaim, Synthesis of a $\text{rGO}/\text{Fe}_3\text{O}_4$ nanoparticle composites and its use as a surface for Alizarin Red S (ARS) dye removal from polluted water, *AIP Conf. Proc.*, 2386 (2022) 030029, doi: 10.1063/5.0069097.
- [46] Md. G. Azam, Md. H. Kabir, Md. A.A. Shaikh, S. Ahmed, M. Mahmud, S. Yasmin, A rapid and efficient adsorptive removal of lead from water using graphene oxide prepared from waste dry cell battery, *J. Water Process Eng.*, 46 (2022) 102597, doi: 10.1016/j.jwpe.2022.102597.
- [47] W. Zou, X. Feng, W. Wei, Y. Zhou, R. Wang, R. Zheng, J. Li, S. Luo, H. Mi, H. Chen, Converting spent LiFePO_4 battery into zeolitic phosphate for highly efficient heavy metal adsorption, *Inorg. Chem.*, 60 (2021) 9496–9503.
- [48] A. Masudi, G.E. Harimisa, N.A. Ghafar, N.W.C. Jusoh, Magnetite-based catalysts for wastewater treatment, *Environ. Sci. Pollut. Res. Int.*, 27 (2020) 4664–4682.
- [49] S.M. Rahimi, A.H. Panahi, N.S. Mazari Moghaddam, E. Allahyari, N. Nasseh, Breaking down of low-biodegradation Acid Red 206 dye using bentonite/ Fe_3O_4 / ZnO magnetic nanocomposite as a novel photo-catalyst in presence of UV light, *Chem. Phys. Lett.*, 794 (2022) 139480, doi: 10.1016/j.cplett.2022.139480.
- [50] H.T. Do, P.H. Nguyen, C.X. Phan, H.N. Nguyen, P.T. Le, T.T.T. Nguyen, T.T. Nguyen, T.N. Pham, M. Osial, T.M.T. Dinh, Hydroxyapatite/superparamagnetic iron oxide nanoparticles nanocomposite for Congo red adsorption, *Desal. Water. Treat.*, (2023) 1–15.
- [51] N. AbouSeada, M.A. Ahmed, M.G. Elmahgary, Synthesis and characterization of novel magnetic nanoparticles for photocatalytic degradation of indigo carmine dye, *Mater. Sci. Energy Technol.*, 5 (2022) 116–124.
- [52] M. Khodadadi, S. Rodriguez-Couto, F.S. Arghavan, A.H. Panahi, Synthesis and characterization of FeNi_3 @ SiO_2 / TiO_2 nanocomposite and its application as a catalyst in a photochemical oxidation process to decompose tetracycline, *Desal. Water Treat.*, 195 (2020) 435–449.
- [53] N. Nasseh, M.T. Samadi, M. Ghadirian, A. Hossein Panahi, A. Rezaie, Photo-catalytic degradation of tamoxifen by using a novel synthesized magnetic nanocomposite of FeCl_2 @ AC/ZnO : a study on the pathway, modeling, and sensitivity analysis using artificial neural network (AAN), *J. Environ. Chem. Eng.*, 10 (2022) 107450, doi: 10.1016/j.jece.2022.107450.
- [54] S.J. Olusegun, N.D.S. Mohalleh, V.S.T. Ciminelli, Reducing the negative impact of ceftriaxone and doxycycline in aqueous solutions using ferrihydrite/plant-based composites: mechanism pathway, *Environ. Sci. Pollut. Res.*, 29 (2022) 66547–66561.
- [55] P. Dhiman, G. Rana, A. Kumar, G. Sharma, D.N. Vo, T.S. AlGarni, Mu. Naushad, Z.A. ALOthman, Nanostructured magnetic inverse spinel Ni–Zn ferrite as environmental friendly visible light driven photo-degradation of levofloxacin, *Chem. Eng. Res. Des.*, 175 (2021) 85–101.
- [56] B. Kakavandi, E. Dehghanifard, P. Gholami, M. Noorisepehr, B.M. Hedayat, Photocatalytic activation of peroxydisulfate by magnetic Fe_3O_4 @ SiO_2 / TiO_2 / rGO core-shell towards degradation and mineralization of metronidazole, *Appl. Surf. Sci.*, 570 (2021) 151145, doi: 10.1016/j.apsusc.2021.151145.
- [57] F. Hayati, M.R. Khodabakhshi, A.A. Isari, S. Moradi, B. Kakavandi, LED-assisted sonocatalysis of sulfathiazole and pharmaceutical wastewater using N,Fe co-doped TiO_2 @SWCNT: optimization, performance and reaction mechanism studies, *J. Water Process Eng.*, 38 (2020) 101693, doi: 10.1016/j.jwpe.2020.101693.
- [58] F.S. Arghavan, A. Hossein Panahi, N. Nasseh, M. Ghadirian, Adsorption-photocatalytic processes for removal of pentachlorophenol contaminant using $\text{FeNi}_3/\text{SiO}_2/\text{ZnO}$ magnetic nanocomposite under simulated solar light irradiation, *Environ. Sci. Pollut. Res.*, 28 (2021) 7462–7475.
- [59] M. Nikazar, M. Alizadeh, R. Lalavi, M. Hossein Rostami, The optimum conditions for synthesis of $\text{Fe}_3\text{O}_4/\text{ZnO}$ core/shell magnetic nanoparticles for photodegradation of phenol, *J. Environ. Health Sci. Eng.*, 12 (2014) 21, doi: 10.1186/2052-336X-12-21.

- [60] S. Akhtar, W. An, X. Niu, K. Li, S. Anwar, K. Maaz, M. Maqbool, L. Gao, Toxicity of PEG-coated CoFe_2O_4 nanoparticles with treatment effect of curcumin, *Nanoscale. Res. Lett.*, 13 (2018) 52, doi: 10.1186/s11671-018-2468-7.
- [61] M. Jouyandeh, M.R. Ganjali, A. Ali, M.J. Aghazadeh, F.J. Stadler, M.R. Saeb, Curing epoxy with electrochemically synthesized CoFe_2O_4 magnetic nanoparticles, *Prog. Org. Coat.*, 137 (2019) 105252, doi: 10.1016/j.porgcoat.2019.105252.
- [62] M.B. Vraneš, S.M. Papović, S.B. Gadžurić, Spectrophotometric investigation of cobalt chloride complex formation in aqueous calcium nitrate–ammonium nitrate melts at $T = 328.15$ K: influence of water content, *J. Solution Chem.*, 48 (2019) 1364–1377.
- [63] Q. Wang, H. Gao, X. Qin, J. Dai, W. Li, Fabrication of NiFe_2O_4 @ CoFe_2O_4 core-shell nanofibers for high-performance supercapacitors, *Mater. Res. Express*, 7 (2020) 015020, doi: 10.1088/2053-1591/ab61ba.
- [64] S. Zhao, D. Ma, Preparation of CoFe_2O_4 nanocrystallites by solvothermal process and its catalytic activity on the thermal decomposition of ammonium perchlorate, *J. Nanomater.*, 2010 (2010) 842816, doi: 10.1155/2010/842816.
- [65] N. Wang, L. Zhu, D. Wang, M. Wang, Z. Lin, H. Tang, Sono-assisted preparation of highly-efficient peroxidase-like Fe_3O_4 magnetic nanoparticles for catalytic removal of organic pollutants with H_2O_2 , *Ultrason. Sonochem.*, 17 (2010) 526–533.
- [66] S.Y. Zhao, D.-G. Lee, C.-W. Kim, H.-G. Cha, Y.-H. Kim, Y.-S. Kang, Synthesis of magnetic nanoparticles of Fe_3O_4 and CoFe_2O_4 and their surface modification by surfactant adsorption, *Bull. Korean Chem. Soc.*, 27 (2006) 237–242.
- [67] S. Ayyappan, S. Mahadevan, P. Chandramohan, P. Srinivasan, J. Philip, B. Raj, Influence of Co^{2+} ion concentration on the size, magnetic properties, and purity of CoFe_2O_4 spinel ferrite nanoparticles, *J. Phys. Chem. C*, 114 (2010) 6334–6341.
- [68] K. Kartha, M. Pai, A. Banerjee, R. Pai, S. Meena, S. Bharadwaj, Modified surface and bulk properties of Fe-substituted lanthanum titanates enhances catalytic activity for $\text{CO} + \text{N}_2\text{O}$ reaction, *J. Mol. Catal. A: Chem.*, 335 (2011) 158–168.
- [69] A.H. Rezaian, M. Mousavi, S. Kheirjou, G. Amoabediny, M.S. Ardestani, J. Mohammadnejad, Monodisperse magnetite (Fe_3O_4) nanoparticles modified with water soluble polymers for the diagnosis of breast cancer by MRI method, *J. Magn. Magn. Mater.*, 420 (2016) 210–217.
- [70] H.R. Dehghanpour, The effects of surfactant changing on physical properties of Fe_3O_4 nanoparticles produced in coprecipitation method, *Russ. J. Inorg. Chem.*, 65 (2020) 1282–1286.
- [71] Y. Li, W. Qiu, F. Qin, H. Fang, V.G. Hadjiev, D. Litvinov, J. Bao, Identification of cobalt oxides with Raman scattering and Fourier transform infrared spectroscopy, *J. Phys. Chem. C*, 120 (2016) 4511–4516.
- [72] M. Ristic, S. Krehula, M. Reissner, M. Jean, B. Hannoyer, S. Musić, Synthesis and properties of precipitated cobalt ferrite nanoparticles, *J. Mol. Struct.*, 1140 (2017) 32–38.
- [73] S. Mitra, P.S. Veluri, A. Chakraborty, R.K. Petla, Electrochemical properties of spinel cobalt ferrite nanoparticles with sodium alginate as interactive binder, *ChemElectroChem*, 1 (2014) 1068–1074.
- [74] R. Rahmani, M. Gharanfoli, M. Gholamin, M. Darroudi, J. Chamani, K. Sadri, A. Hashemzadeh, Plant-mediated synthesis of superparamagnetic iron oxide nanoparticles (SPIONs) using aloe vera and flaxseed extracts and evaluation of their cellular toxicities, *Ceram. Int.*, 46 (2020) 3051–3058.
- [75] P. Pietrzyk, N.T. Phuong, S.J. Olusegun, N. Hong Nam, D.T.M. Thanh, M. Giersig, P. Krysiński, M. Osial, Titan yellow and Congo red removal with superparamagnetic iron-oxide-based nanoparticles doped with zinc, *Magnetochemistry*, 8 (2022) 91, doi: 10.3390/magnetochemistry8080091.
- [76] D.T.M. Thanh, N.T. Phuong, D.T. Hai, H.N. Giang, N.T. Thom, P.T. Nam, N.T. Dung, M. Giersig, M. Osial, Influence of experimental conditions during synthesis on the physicochemical properties of the SPION/hydroxyapatite nanocomposite for magnetic hyperthermia application, *Magnetochemistry*, 8 (2022) 90, doi: 10.3390/magnetochemistry8080090.
- [77] J. Kundu, D. Pradhan, Controlled synthesis and catalytic activity of copper sulfide nanostructured assemblies with different morphologies, *ACS Appl. Mater. Interfaces*, 6 (2014) 1823–1834.
- [78] A.J. Deotale, R.V. Nandedkar, Correlation between particle size, strain and band gap of iron oxide nanoparticles, *Mater. Today Proc.*, 3 (2016) 2069–2076.
- [79] V.S. Kirankumar, S. Sumathi, Photocatalytic and antibacterial activity of bismuth and copper co-doped cobalt ferrite nanoparticles, *J. Mater. Sci. - Mater. Electron.*, 29 (2018) 8738–8746.
- [80] Y. Yao, G. Wu, F. Lu, S. Wang, Y. Hu, J. Zhang, W. Huang, F. Wei, Enhanced photo-Fenton-like process over Z-scheme CoFe_2O_4 /g- C_3N_4 heterostructures under natural indoor light, *Environ. Sci. Pollut. Res.*, 23 (2016) 21833–21845.
- [81] P.J. Costa, The halogen bond: nature and applications, *Phys. Sci. Rev.*, 2 (2017) 1–16.
- [82] R.G. Pearson, Hard and soft acids and bases—the evolution of a chemical concept, *Coord. Chem. Rev.*, 100 (1990) 403–425.
- [83] I. Fleming, *Molecular Orbitals and Organic Chemical Reactions*, John Wiley & Sons, London, 1976.
- [84] M.J. Frisch, G.W. Trucks, H.B. Schlegel, G.E. Scuseria, M.A. Robb, J.R. Cheeseman, Gaussian 09, Revision C.02, Gaussian Inc., Wallingford CT, 2010.
- [85] A.O. Elzupir, R.K. Hussein, K.H. Ibaouf, Intermolecular $\text{CH}-\pi$ electrons interaction in poly(9,9-dioctylfluorenyl-2,7-diyl) (PFO): an experimental and theoretical study, *Molecules*, 27 (2022) 1488, doi: 10.3390/molecules27051488.
- [86] K. Raghavachari, Perspective on “Density functional thermochemistry. III. The role of exact exchange”, *Theor. Chem. Acc.*, 103 (2000) 361–363.
- [87] S.K. Alghamdi, F. Abbas, R.K. Hussein, A.G. Alhamzani, N.T. El-Shamy, Spectroscopic characterization (IR, UV-Vis), and HOMO-LUMO, MEP, NLO, NBO analysis and the antifungal activity for 4-bromo-N-(2-nitrophenyl) benzamide; using DFT modeling and in silico molecular docking, *J. Mol. Struct.*, 1271 (2023) 13400.
- [88] S. Swapna Priya, K.V. Radha, A review on the adsorption studies of tetracycline onto various types of adsorbents, *Chem. Eng. Commun.*, 204 (2017) 821–839.
- [89] S.J. Olusegun, G. Larrea, M. Osial, K. Jackowska, P. Krysiński, Photocatalytic degradation of antibiotics by superparamagnetic iron oxide nanoparticles, Tetracycline case, *Catalysts*, 11 (2021) 1243, doi: 10.3390/catal11101243.
- [90] Y. Wang, J. Xiu, T. Gan, H. Zou, F. Li, Photocatalytic degradation of tetracycline hydrochloride by lanthanum doped TiO_2 @g- C_3N_4 activated persulfate under visible light irradiation, *RSC Adv.*, 13 (2023) 8383–8393.
- [91] A. Hemmi, M. Belmedani, E. Mekatel, R. Brahimi, M. Trari, Kinetic and mechanism studies of tetracycline photodegradation using synthesized ZnAl_2O_4 , *React. Kinet. Mech. Catal.*, 134 (2021) 1039–1054.
- [92] W. Piasecki, K. Szymonek, R. Charnas, Fe^{2+} adsorption on iron oxide: the importance of the redox potential of the adsorption system, *Adsorption*, 25 (2019) 613–619.
- [93] M.E. Peralta, R. Nisticò, F. Franzoso, G. Magnacca, L. Fernandez, M.E. Parolo, E.G. León, L. Carlos, Highly efficient removal of heavy metals from waters by magnetic chitosan-based composite, *Adsorption*, 25 (2019) 1337–1347.
- [94] H. Wang, C. Fang, Q. Wang, Y. Chu, Y. Song, Y. Chen, X. Xue, Sorption of tetracycline on biochar derived from rice straw and swine manure, *RSC Adv.*, 8 (2018) 16260–16268.
- [95] A. Samadi-Maybodi, R. Khabazifard, Photodegradation of tetracycline and doxycycline under visible radiation using MIL-MIL101Fe (NH_4)@g- C_3N_4 @ CoFe_2O_4 /GO as photocatalyst, *Optik*, 262 (2022) 168934, doi: 10.1016/j.ijleo.2022.168934.
- [96] L. Zhang, X. Song, X. Liu, L. Yang, F. Pan, J. Lv, Studies on the removal of tetracycline by multiwalled carbon nanotubes, *Chem. Eng. J.*, 178 (2011) 26–33.
- [97] J.-Z. Kong, A.-D. Li, X.-Y. Li, H.-F. Zhai, W.-Q. Zhang, Y.-P. Gong, H. Li, D. Wu, Photo-degradation of methylene blue using Ta-doped ZnO nanoparticle, *J. Solid State Chem.*, 183 (2010) 1359–1364.

- [98] H. Yuan, Q. Su, Y. Wang, J. Li, B. Liu, Y. Li, P. Wu, Tetracycline catalytic photodegradation with mesoporous phosphated TiO₂: characterization, process optimization and degradation pathway, *RSC Adv.*, 11 (2021) 10975–10985.
- [99] A.P. Farheen, Enhanced visible light energy harvesting and efficient photocatalytic antibiotic drug degradation over egg albumen mediated Sr doped Fe₂O₃ nanoparticles, *Mater. Sci. Semicond. Process.*, 148 (2022) 106804, doi: 10.1016/j.mssp.2022.106804.
- [100] M. Nagamine, M. Osial, K. Jackowska, P. Krysinski, J. Widera-Kalinowska, Tetracycline photocatalytic degradation under CdS treatment, *J. Mar. Sci. Eng.*, 8 (2020) 483, doi: 10.3390/jmse8070483.
- [101] S.-Y. Liu, A. Zada, X. Yu, F. Liu, G. Jin, NiFe₂O₄/g-C₃N₄ heterostructure with an enhanced ability for photocatalytic degradation of tetracycline hydrochloride and antibacterial performance, *Chemosphere*, 307 (2022) 135717, doi: 10.1016/j.chemosphere.2022.135717.
- [102] C. Lai, F. Xu, M. Zhang, B. Li, S. Liu, H. Yi, L. Li, L. Qin, X. Liu, Y. Fu, Y. An, N. An, H. Yang, X. Huo, X. Yang, H. Yan, Facile synthesis of CeO₂/carbonate doped Bi₂O₂CO₃ Z-scheme heterojunction for improved visible-light photocatalytic performance: photodegradation of tetracycline and photocatalytic mechanism, *J. Colloid Interface Sci.*, 588 (2021) 283–294.
- [103] S.J. Singh, P. Chinnamuthu, Magnetically recoverable Cu_(1-x)Ce_xO nanoparticles for photodegradation of tetracycline, *Colloids Surf., A*, 656 (2023) 130404, doi: 10.1016/j.colsurfa.2022.130404.
- [104] P. Semeraro, S. Bettini, S. Sawalha, S. Pal, A. Licciulli, F. Marzo, N. Lovergine, L. Valli, G. Giancane, Photocatalytic degradation of tetracycline by ZnO/γ-Fe₂O₃ paramagnetic nanocomposite material, *Nanomaterials*, 10 (2020) 1458, doi: 10.3390/nano10081458.
- [105] B. Kakavandi, S. Alavi, F. Ghanbari, M. Ahmadi, Bisphenol A degradation by peroxymonosulfate photo-activation coupled with carbon-based cobalt ferrite nanocomposite: performance, upgrading synergy and mechanistic pathway, *Chemosphere*, 287 (2022) 132024, doi: 10.1016/j.chemosphere.2021.132024.
- [106] A.A. Isari, S. Moradi, S.S. Rezaei, F. Ghanbari, E. Dehghanifard, B. Kakavandi, Peroxymonosulfate catalyzed by core/shell magnetic ZnO photocatalyst towards malathion degradation: enhancing synergy, catalytic performance and mechanism, *Sep. Purif. Technol.*, 275 (2021), 119163, doi: 10.1016/j.seppur.2021.119163.
- [107] J. Wang, F. Osterloh, Limiting factors for photochemical charge separation in BiVO₄/Co₃O₄, a highly active photocatalyst for water oxidation in sunlight, *J. Mater. Chem. A*, 2 (2014) 9405–9411.
- [108] F. Hu, W. Luo, C. Liu, H. Dai, X. Xu, Q. Yue, L. Xu, G. Xu, Y. Jian, X. Peng, Fabrication of graphitic carbon nitride functionalized P-CoFe₂O₄ for the removal of tetracycline under visible light: optimization, degradation pathways and mechanism evaluation, *Chemosphere*, 274 (2021) 129783, doi: 10.1016/j.chemosphere.2021.129783.
- [109] S. Giannakis, S. Liu, A. Carratalà, S. Rtimi, M.T. Amiri, M. Bensimon, C. Pulgarin, Iron oxide-mediated semiconductor photocatalysis vs. heterogeneous photo-Fenton treatment of viruses in wastewater. Impact of the oxide particle size, *J. Hazard. Mater.*, 339 (2017) 223–231.
- [110] Y. Nosaka, A. Nosaka, Understanding hydroxyl radical (•OH) generation processes in photocatalysis, *ACS Energy Lett.*, 1 (2016) 356–359.
- [111] D. Lawless, N. Serpone, D. Meisel, Role of hydroxyl radicals and trapped holes in photocatalysis. A pulse radiolysis study, *J. Phys. Chem.*, 95 (1991) 5166–5170.
- [112] M.L. Kremer, Mechanism of the Fenton reaction. Evidence for a new intermediate, *Phys. Chem. Chem. Phys.*, 1 (1999) 3595–3605.
- [113] A.V. Vorontsov, Advancing Fenton and photo-Fenton water treatment through the catalyst design, *J. Hazard. Mater.*, 372 (2019) 103–112.
- [114] K. Du, E.H. Ang, X. Wu, Y. Liu, Progresses in sustainable recycling technology of spent lithium-ion batteries, *Energy Environ. Mater.*, 5 (2022) 1012–1036.
- [115] X. He, T. Kai, P. Ding, Heterojunction photocatalysts for degradation of the tetracycline antibiotic: a review, *Environ. Chem. Lett.*, 19 (2021) 4563–4601.
- [116] P. Meshram, A. Mishra, Abhilash, R. Sahu, Environmental impact of spent lithium ion batteries and green recycling perspectives by organic acids – a review, *Chemosphere*, 242 (2020) 125291, doi: 10.1016/j.chemosphere.2019.125291.
- [117] Z. Dobó, T. Dinh, T. Kulcsár, A review on recycling of spent lithium-ion batteries, *Energy Rep.*, 9 (2023) 6362–6395.
- [118] J. Zhang, Chapter 10 – Application of Hydrometallurgy in Spent Lithium-Ion Battery Recycling, S. Farhad, R.K. Gupta, G. Yasin, T.A. Nguyen, Micro and Nano Technologies, Nano Technology for Battery Recycling, Remanufacturing, and Reusing, Elsevier, Denmark, 2022, pp. 183–216.
- [119] Y. Ma, J. Tang, R. Wanaldi, X. Zhou, H.C. Wang, Zhou, J. Yang, A promising selective recovery process of valuable metals from spent lithium-ion batteries via reduction roasting and ammonia leaching, *J. Hazard. Mater.*, 402 (2021) 123491, doi: 10.1016/j.jhazmat.2020.123491.
- [120] S.T. Yan, R.Z. Wang, C.Y. Shao, Z.Q. Tong, T. Li, L.J. Yuan, G.H. Sheng, K.X. Xu, The strategy of entire recovery: from spent cathode material with high nickel content to new LiNi_{0.5}Co_{0.2}Mn_{0.3}O₂ and Li₂CO₃ powders, *J. Power Sources*, 440 (2019) 227140, doi: 10.1016/j.jpowsour.2019.227140.
- [121] D. Patil, S. Chikkamath, S. Keny, V. Tripathi, J. Manjanna, Rapid dissolution and recovery of Li and Co from spent LiCoO₂ using mild organic acids under microwave irradiation, *J. Environ. Manage.*, 15 (2020) 109935, doi: 10.1016/j.jenvman.2019.109935.
- [122] Y. Zhang, Recycling of cathode material from spent lithium-ion batteries using an ultrasound-assisted DL-malic acid leaching system, *Waste Manage.*, 15 (2020) 52–60.
- [123] Y.P. Fu, Y.Q. He, Y. Yang, L.L. Qu, J.L. Li, R. Zhou, Microwave reduction enhanced leaching of valuable metals from spent lithium-ion batteries, *J. Alloys Compd.*, 832 (2020) 154920, doi: 10.1016/j.jallcom.2020.154920.
- [124] Y. Zhao, B. Liu, L. Zhang, S. Guo, Microwave pyrolysis of macadamia shells for efficiently recycling lithium from spent lithium-ion batteries, *J. Hazard. Mater.*, 5 (2020) 122740, doi: 10.1016/j.jhazmat.2020.122740.
- [125] P. Giorgio Schiavi, P. Altimari, M. Branchi, R. Zanon, G. Simonetti, M. Assunta Navarra, F. Pagnanelli, Selective recovery of cobalt from mixed lithium-ion battery wastes using deep eutectic solvent, *Chem. Eng. J.*, 417 (2021) 129249, doi: 10.1016/j.cej.2021.129249.
- [126] A. Pęgowska, M. Osial, W. Urbańska, The application of artificial intelligence in the effective battery life cycle in the closed circular economy model—a perspective, *Recycling*, 7 (2022) 81, doi: 10.3390/recycling7060081.
- [127] C. Ruhatiya, S. Shaosen, C.-T. Wang, A.K. Jishnu, Y. Bhalerao, Optimization of process conditions for maximum metal recovery from spent zinc-manganese batteries: illustration of statistical based automated neural network approach, *Energy Storage, Special Issue: Renewable Energy and Energy Storage Systems*, 2 (2020) e111, doi: 10.1002/est.111.
- [128] M. Noor, M.H. Wong, S. Ngadi, I.M. Inuwa, L.A. Opotu, Assessing the effectiveness of magnetic nanoparticles coagulation/flocculation in water treatment: a systematic literature review, *Int. J. Environ. Sci. Technol.*, 19 (2020) 6935–6956.
- [129] S. Shukla, R. Khan, A. Daverey, Synthesis and characterization of magnetic nanoparticles, and their applications in wastewater treatment: a review, *Environ. Technol. Innovation*, 24 (2021) 10192, doi: 10.1016/j.eti.2021.101924.
- [130] F. Gao, An overview of surface-functionalized magnetic nanoparticles: preparation and application for wastewater treatment, *ChemistrySelect*, 4 (2019) 6805–6811.
- [131] A.E. Vasu, A.P. Mary Sri Archana, A.C. Sagayaraj, F.F. Reymond, V.A. Jasmine, A.T. Elizabeth, Magnetic nanocomposite fabrication using banana leaf sheath biofluid:

- enhanced Fenton catalytic activity towards tetracycline degradation, *Inorg. Chem. Commun.*, 141 (2022) 109541, doi: 10.1016/j.inoche.2022.109541.
- [132] Y.C. Sharma, V. Srivastava, Comparative studies of removal of Cr(VI) and Ni(II) from aqueous solutions by magnetic nanoparticles, *J. Chem. Eng. Data*, 56 (2011) 819–825.
- [133] S. Zhang, Y. Zhang, G. Bi, J. Liu, Z. Wang, Q. Xu, H. Xu, X. Li, Mussel-inspired polydopamine biopolymer decorated with magnetic nanoparticles for multiple pollutants removal, *J. Hazard. Mater.*, 270 (2014) 27–34.
- [134] K. Chen, J. He, Y. Li, X. Cai, K. Zhang, T. Liu, Y. Hu, D. Lin, L. Kong, J. Liu, Removal of cadmium and lead ions from water by sulfonated magnetic nanoparticle adsorbents, *J. Colloid Interface Sci.*, 494 (2017) 307–316.
- [135] G.T. Tee, X.T. Gok, W.F. Yong, Adsorption of pollutants in wastewater via biosorbents, nanoparticles and magnetic biosorbents: a review, *Environ. Res.*, 212 (2022) 113248, doi: 10.1016/j.envres.2022.113248.
- [136] S. Karimi, H. Namazi, Magnetic alginate/glycodendrimer beads for efficient removal of tetracycline and amoxicillin from aqueous solutions, *Int. J. Biol. Macromol.*, 205 (2022) 128–140.
- [137] Z. Alizadeh, A. Rezaee, Tetracycline removal using microbial cellulose@nano-Fe₃O₄ by adsorption and heterogeneous Fenton-like processes, *J. Mol. Liq.*, 366 (2022) 120199, doi: 10.1016/j.molliq.2022.120199.
- [138] L. Zhang, Y. Wang, Y. Shi, Y. Zhu, Heterogeneous catalytic oxidation of tetracycline hydrochloride based on persulfate activated by Fe₃O₄/MC composite, *Chem. Eng. J.*, 447 (2022) 137406, doi: 10.1016/j.cej.2022.137406.
- [139] A. Nasiri, S. Rajabi, A. Amiri, M. Fattahizade, O. Hasani, A. Lalehzari, M. Hashemi, Adsorption of tetracycline using CuCoFe₂O₄@chitosan as a new and green magnetic nanohybrid adsorbent from aqueous solutions: isotherm, kinetic and thermodynamic study, *Arabian J. Chem.*, 15 (2022) 104014, doi: 10.1016/j.arabjc.2022.104014.
- [140] H. Zhu, A. Guo, S. Wang, Y. Long, G. Fan, X. Yu, Efficient tetracycline degradation via peroxymonosulfate activation by magnetic Co/N co-doped biochar: emphasizing the important role of biochar graphitization, *Chem. Eng. J.*, 450 (2022) 138428, doi: 10.1016/j.cej.2022.138428.
- [141] M. Usman, A. Ahmed, Z. Ji, B. Yu, M. Rafiq, Y. Shen, H. Cong, Enhanced heterogenous photo-Fenton degradation of tetracycline in aqueous medium by visible light responsive sulphur doped zinc ferrite nanoparticles, *Mater. Today Chem.*, 26 (2022) 101003, doi: 10.1016/j.mtchem.2022.101003.
- [142] U. Kumar, J. Kuntail, A. Kumar, R. Prakash, M.R. Pai, I. Sinha, *In-situ* H₂O₂ production for tetracycline degradation on Ag/s-(Co₃O₄/NiFe₂O₄) visible light magnetically recyclable photocatalyst, *Appl. Surf. Sci.*, 589 (2022) 153013, doi: 10.1016/j.apsusc.2022.153013.